Geophys. J. Int. (2009) **177,** 783–805 doi: 10.1111/j.1365-246X.2008.04024.x

Late Cenozoic volcanism and rates of active faulting in eastern Iran

R. T. Walker,[1] P. Gans,[2] M. B. Allen,[3] J. Jackson,[4] M. Khatib,[5] N. Marsh[6] and M. Zarrinkoub[5]

[1]*Department of Earth Sciences, University of Oxford, Parks Road, Oxford,* OX1 3PR*, UK. E-mail: richw@earth.ox.ac.uk*
[2]*Department of Earth Sciences, University of California, Santa Barbara,* CA 93106*, USA*
[3]*Department of Earth Sciences, Science Labs, University of Durham, Durham,* DH1 3LE*, UK*
[4]*Bullard Laboratories, Madingley Road, Cambridge,* CB3 0EZ*, UK*
[5]*Department of Geology, Birjand University, Birjand, Iran*
[6]*Department of Earth Sciences, University of Leicester, University Road, Leicester,* LE1 7RH*, UK*

Accepted 2008 October 20. Received 2008 October 19; in original form 2008 April 18

SUMMARY

We present new $^{40}Ar/^{39}Ar$ ages of samples of volcanic rock exposed along the remote margins of the Dasht-e Lut desert in eastern Iran. Close spatial relationships between the volcanic rocks and the trace of active strike-slip faults allow us to determine the slip rates of two major faults, averaged since eruption of the volcanics. Our study shows that the Nayband fault at the western margin of the Dasht-e Lut has a slip rate of $\sim 1.4 \pm 0.5$ mm yr^{-1} averaged over 2.25 Ma. The East Neh fault, one of several active strike-slip faults within the Sistan Suture Zone at the eastern margin of the Dasht-e Lut, has a minimum slip rate of ~ 1.2 mm yr^{-1} averaged over ~ 1.7 Ma. The rates of slip on major active faults in eastern Iran are largely unknown, and the slip rates our data provide, though limited, are a significant increase on what is known of the faulting within this remote and relatively inaccessible desert region. We also present analyses of the major and trace element concentrations within the volcanic rocks. The chemistry of the volcanic rocks is typical of intracontinental melts with an overall signature similar to that of ocean island basalts. Inversion of rare earth element distributions suggests some melting has occurred at depths of ~ 80 km, indicating the presence of a relatively thin lithosphere beneath eastern Iran, in agreement with recently published maps of lithospheric thickness derived from shear wave velocities.

Key words: Intra-plate processes; Continental tectonics: strike-slip and transform; Rheology: crust and lithosphere; Asia.

1 INTRODUCTION

This paper concerns the ways in which tectonic deformation is distributed on active strike-slip faults in eastern Iran. Iran is deforming due to the Arabia–Eurasia collision and has a long record of destructive earthquake events (e.g. Ambraseys & Melville 1982; Berberian & Yeats 1999). Despite the abundance of destructive earthquakes, we have very little data on the rates at which individual faults in Iran are moving: information that would be beneficial both for studies of the regional seismic hazard and for studies of the kinematics of continental deformation in Iran. In addition, there has recently been a debate as to whether slip rates in regions of strike-slip faulting are constant through time or whether activity switches between parallel active faults on timescales of several thousand years (e.g. Dolan *et al.* 2007). Meyer & Le Dortz (2007) propose such a scenario for central and eastern Iran (Fig. 1), with activity switching between faults that surround the Dasht-e Lut (and which are shown by GPS measurements to be moving rapidly at the present day) and faults that are situated further west in central Iran (which show evidence for Holocene activity, but are not discernible in the GPS velocity field).

If the scenario of Meyer & Le Dortz (2007) is correct, it has major implications for whether short-term (geodetic) and long-term (late Quaternary and geological) estimates of slip on faults in Iran are comparable. Testing whether fault slip rates in Iran are constant or variable requires detailed information on the rates of faults averaged over various timescales. However, the available GPS coverage is, in most parts of Iran, too coarse to measure strain accumulation across individual structures, and studies that quantify fault slip rates over late Quaternary timescales are rare (exceptions include Regard *et al.* 2005; Fattahi *et al.* 2006, 2007). Instead, most of our existing constraints on fault slip rates come from estimating the total displacements of geological or geomorphological units across the active faults and dividing by an assumed age of those offsets (e.g. Talebian & Jackson 2002; Walker & Jackson 2004; Copley and Jackson 2006; Hollingsworth *et al.* 2006; Meyer *et al.* 2006; Meyer & Le Dortz 2007).

In this paper, we provide $^{40}Ar/^{39}Ar$ age constraints for several volcanic centres displaced by major strike-slip faults around the Dasht-e Lut desert in eastern Iran. Our new age constraints allow us to provide the first quantitative estimates of the slip rates on two

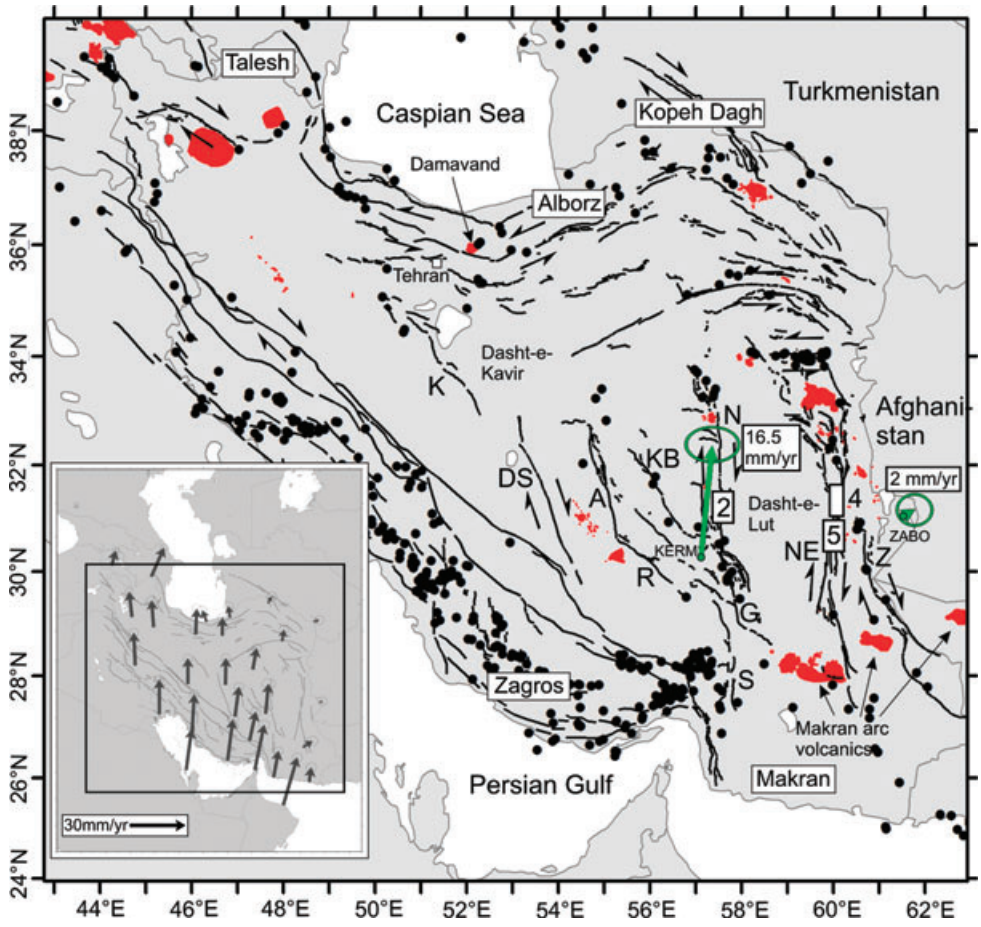

Figure 1. Map of Iran showing the distribution of active faults, earthquake epicentres (magnitude >5, from the catalogue of Engdahl *et al.* 1998 and its subsequent updates) and outcrops of Plio-Quaternary volcanic rocks (from Emami *et al.* 1993). Plio-Quaternary volcanism (marked in red) is widespread across eastern and central parts of the country. An east–west alignment in active volcanoes north of the Makran mountains represents volcanism from active subduction of oceanic lithosphere of the Arabian sea. Volcanic centres within the interior of Iran appear to show either an NW–SE alignment or appear to be closely associated with zones of presently active faulting (for instance, around the Dasht-e Lut desert). GPS velocities of points relative to Eurasia, shown in the inset, are from Vernant *et al.* (2004). The GPS velocities (relative to Eurasia) of stations KERM and ZABO, which together define the 16 ± 2 mm yr^{-1} rate of north–south right-lateral shear across eastern Iran, are included on the main map for clarity (in green). Active faults are labelled as follows: Z = Zahedan; NE = Neh faults (East and West Neh); S = Sabzevaran; G = Gowk; N = Nayband; KB = Kuh Banan; R = Rafsanjan; A = Anar; DS = Deh Shir; K = Kashan. The Neh and Zahedan faults east of the Dasht-e Lut desert are situated within the Sistan Suture Zone.

major faults in eastern Iran averaged over the last few million years. We then compare our measured rates with the late Quaternary slip rates inferred across individual faults (Meyer *et al.* 2006; Meyer & Le Dortz 2007).

Plio-Quaternary volcanic rocks are widespread across the interior of Iran and Anatolia (e.g. Fig. 1; Pearce *et al*. 1990; Keskin *et al.* 1998; Almandaz *et al.* 2000). Our eight samples are from remote parts of eastern Iran with very limited access in the field. The new information on the age and composition of these rocks provides insights into the tectonic processes and evolution of Iran. We therefore combine our dating work with an analysis of the chemical composition and the likely origin of volcanism within this poorly known region.

2 TECTONIC SETTING OF THE DASHT-E LUT AND SURROUNDINGS

The deformation of Iran results from convergence between Arabia – Eurasia. The initial Arabia–Eurasia continental collision probably dates from as early as ∼35 Ma (e.g. Agard *et al*. 2005; Vincent *et al*. 2005). A velocity field for Iran, generated from repeated GPS measurements, demonstrates the regional distribution of present-day deformation (Fig. 1; Vernant *et al.* 2004). Both the GPS and the distribution of earthquakes show that shortening in Iran is accommodated by distributed faulting in high mountain ranges in the south (the Zagros) and the north (the Alborz and Kopeh Dagh) of the country (Fig. 1). Surrounding regions to the north (Turkmenistan) and the east (western Afghanistan and Pakistan) are aseismic and appear to be deforming at much lower rates at the present day (e.g. Vernant *et al.* 2004).

The N–NNE motion of central parts of Iran relative to Afghanistan results in north–south (N–S) right-lateral shear of ∼16 mm yr^{-1} at the present day in eastern Iran between the longitudes 56°E and 62°E (Vernant *et al.* 2004). North of 34°N, left-lateral strike-slip faults are thought to take up the right-lateral shear by rotating clockwise (e.g. Jackson & McKenzie 1984; Walker *et al.* 2004; Allen *et al.* 2006; see Fig. 1). South of 34°N, right-lateral shear is accommodated on a series of parallel N–S right-lateral faults running along the eastern margin (the Sistan Suture Zone fault systems) and the western margin (the Nayband–Gowk–Sabzevaran fault

Table 1. A summary of the measured and inferred rates of slip on the strike-slip faults of central and eastern Iran.

	Deh Shir	Anar	Kuh Banan	Nayband	Gowk	Sabzevaran	West Neh	East Neh	Zahedan
Geological offset (km)	65 ± 15	25 ± 5			12–15		∼10	∼50	13–20
Measured long-term slip rate (mm yr^{-1})				∼0.9–1.9				>1.2	
Measured Holocene rate (mm yr^{-1})						4.0–7.4			
Inferred Holocene rate (mm yr^{-1})	∼2	0.50–0.75					1–5		1.75–2.50
Present-day (GPS) rate (mm yr^{-1})						0.6–5.6			

All the faults are labelled in Fig. 1. Measurements of total geological slip are from Meyer *et al.* (2006) for the Deh Shir fault, Meyer & Le Dortz (2007) for the Anar fault and Walker & Jackson (2004) for all other values. The measured long-term slip rates are from this paper. The measured Holocene slip rate on the Sabzevaran fault is from Regard *et al.* (2005). Inferred Holocene rates are from Meyer & Le Dortz (2007). The GPS-derived slip rate for the Sabzevaran fault is from Bayer *et al.* (2006).

system) of the Dasht-e Lut (Fig. 1). The Dasht-e Lut is a low-lying and aseismic desert depression, and little is known of its bedrock composition and structure. A number of additional major right-lateral strike-slip faults are found west of the Nayband–Gowk–Sabzevaran system in central Iran (Fig. 1). These faults, which include the Kuh Banan, Anar, Deh Shir and Kashan faults, all display evidence for activity in the late Quaternary (e.g. Berberian 1976; Walker & Jackson 2004; Meyer *et al.* 2006; Meyer & Le Dortz 2007). However, the existing GPS velocities in eastern Iran are not, in general, sufficient to determine the rate of movement across any of the individual right-lateral faults (Vernant *et al.* 2004).

An initial attempt to determine the distribution of slip on faults across eastern Iran was made by Walker & Jackson (2004). They measured geological and geomorphological estimates of total fault offsets and found that the total right-lateral shear on faults east of the Dasht-e Lut (in the Sistan Suture Zone) is much greater than the total amounts of shear at the western margin of the Lut (∼70–80 km of shear along the eastern margin, and ∼20 km of shear in the west; see Table 1). By assuming that the distribution of geological slip is representative of that occurring at the present day, they inferred that over two-thirds (>10 mm yr^{-1}) of the 15 mm yr^{-1} rate of right-lateral shear between Iran and Afghanistan is accommodated across faults in the Sistan Suture Zone. Within the uncertainty of the GPS measurements (1–2 mm yr^{-1}), no present-day deformation is apparent within the central Iranian plateau (Vernant *et al.* 2004). Walker & Jackson (2004) therefore suggested that the proportion of the ∼16 mm yr^{-1} rate of right-lateral shear accommodated on the Deh Shir and Anar faults of central Iran is also negligible when averaged over longer timescales. The clearly visible scarps on the Deh Shir and Anar fault (e.g. Berberian 1976) do, however, suggest that the faults have been active in the late Quaternary, prompting Walker & Jackson (2004) to suggest that recent activity on the right-lateral faults of central Iran might instead be caused by the accommodation of N–S shortening (at a maximum rate of 2 mm yr^{-1} allowed in the GPS uncertainties) by a combination of right-lateral strike-slip and anticlockwise, vertical-axis rotation of crustal material. Following the model of Walker & Jackson (2004), the ∼100 km of right-lateral slip measured from geological offsets around the Dasht-e Lut can be accounted for in only 6–7 Ma at the ∼16 mm yr^{-1} rate inferred from the GPS velocities. Walker & Jackson (2004) then suggested that the large displacements on strike-slip faults within the central Iranian plateau are likely to have accumulated in an earlier part of the tectonic history. An initiation of the faulting around the Dasht-e Lut at 6–7 Ma agrees well with the observation that many of the deforming belts in the Iran region appear to have either initiated or gone through a major reorganization in structure at ∼3–7 Ma (e.g. Axen *et al.* 2001; Allen *et al.* 2004).

However, several recent studies suggest that some of the Iranian deforming zones initiated substantially earlier than 3–7 Ma. Verdel *et al.* (2007) suggest the initiation of shortening in central Iran at ∼20 Ma. Rapid exhumation in the Alborz may have started at ∼12 Ma (Guest *et al.* 2006). Also, Hollingsworth *et al.* (2006) suggest that active faulting in the Kopeh Dagh started at ∼10 Ma (though this estimate relies on an extrapolation of the GPS shortening rates to account for the observed geological displacements across the faults rather than directly dating the onset of faulting and mountain building).

Fault slip rates constrained by analytical dating techniques are rare in eastern Iran (see Table 1). Walker & Jackson (2002) suggested a ∼1.5 mm yr^{-1} slip rate on the Nayband fault from a ∼3 km offset of a Quaternary basalt flow (this slip-rate estimate is reassessed in Section 4.1). The only other quantitative slip-rate determination in the Dasht-e Lut region is for the Sabzevaran fault (Fig. 1). Regard *et al.* (2005) estimated a rate of ∼4.0–7.4 mm yr^{-1} of right-lateral slip on this fault from exposure dating of boulders set within displaced alluvial fans. The most recent extensive period of alluvial deposition across the Sabzevaran fault was dated by Regard *et al.* (2005) at 12 ± 2 Ka. A similar age of ∼10 Ka for the abandonment of alluvial fans was found at two sites in northeastern (NE) Iran (Fattahi *et al.* 2006, 2007), supporting the hypothesis that alluvial fan abandonment was synchronous, and presumably controlled by a regional change in climate, around the start of the Holocene.

Meyer & Le Dortz (2007) analysed high-resolution SPOT 5 and Quickbird satellite imagery to identify young alluvial fan deposits displaced by strike-slip faults in eastern and central Iran. Restoration of the fan displacements, combined with an assumption that they date from 12 ± 2 Ka, yielded slip-rate estimates (from east to west) of 1.75–2.50 mm yr^{-1} for the East Neh fault, 1.0–2.5 mm yr^{-1} for the Asagie fault (the southern continuation of the East Neh fault), 1–5 mm yr^{-1} for the West Neh fault and ∼0.50–0.75 mm yr^{-1} for the Anar fault (see Table 1). A similar approach by Meyer *et al.* (2006) yielded an assumed Holocene slip rate of ∼2 mm yr^{-1} for the Deh Shir fault. All of these slip-rate estimates are within the uncertainties of the velocity field derived from the GPS and are therefore compatible with it.

Although the Deh Shir and Anar faults of Iran were previously recognized as active in the late Quaternary (Berberian 1976; Walker & Jackson 2004), the lack of deformation imaged by the GPS and the overall absence of seismicity in central Iran had led to the strike-slip faults being neglected in models of the kinematics of eastern Iran (Walker & Jackson 2004). Using their slip-rate estimates, Meyer & Le Dortz (2007) suggested that, when averaged over the last 10 Ka, the 16 mm yr^{-1} rate of right-lateral shear between Iran and Afghanistan is accommodated over a region much wider than apparent from the geodetically measured distribution of strain. If the 16 mm yr^{-1} rate of right-lateral shear between Iran and Afghanistan is accommodated over Holocene timescales across

the entire width of eastern and central Iran, the GPS measurements of right-lateral shear across eastern Iran cannot be extrapolated to long-term measurements of slip on the major faults, and the cumulative displacements of bedrock geology mapped by Walker & Jackson (2004) would require much longer than 6–7 Ma to accumulate (between 8 and 22 Ma, according to Meyer & Le Dortz, 2007).

There are, however, several remaining uncertainties in the model of Meyer & Le Dortz (2007). First, they only estimated the rates in four of the major right-lateral strike-slip faults of eastern and central Iran (Table 1). The contributions of the Zahedan, Kuh Banan and Kashan faults are not included in their model, precluding a complete description of the distribution of slip across eastern Iran. Also, the role of the Deh Shir and Anar faults in the regional tectonics is not fully understood. Walker and Jackson (2004) suggest that, rather than simply translating material by N–S right-lateral shear, their activity results from the accommodation of small amounts of N–S shortening by a combination of right-lateral slip and anticlockwise, vertical-axis rotation. If the Deh Shir and Anar faults accommodate shortening by rotation, their slip rates cannot be summed to determine the rates of regional shearing. Finally, the assumption that young alluvial fans can be confidently assigned an age of 12 ± 2 Ka across large areas of eastern Iran is not yet tested. To properly validate the slip rates of Meyer & Le Dortz (2007), one requires quantitative age estimates from each of the displaced alluvial fans that they observed in high-resolution satellite imagery. One of the aims of our paper is to see whether fault slip rates averaged over million-year timescales agree with the inferred Holocene rates of Meyer & Le Dortz (2007). This comparison is made in Section 4.3.

3 METHODS

3.1 $^{40}Ar/^{39}Ar$ dating

$^{40}Ar/^{39}Ar$ age determinations were obtained from seven of the eight samples. The ages are presented in Table 2. Errors reported on plateau ages are ±2 sigma. Additional information, including tabulated analytical data, age and K/Ca spectra and inverse isochron plots for these samples are provided in Appendix.

Table 2. Sample locations and $^{40}Ar/^{39}Ar$ age determinations.

Sample no.	Latitude	Longitude	Age (Ma)
Nayband			
1	31:22:18	57:31:07	2.60 ± 0.20
2	31:21:34	57:31:28	2.20 ±−0.05
3	31:04:21	57:35:04	2.25 ± 0.06
East Neh			
AVNEH	31:19:08	60:09:26	1.60 ± 0.15
BVNEH	31:19:58	60:07:33	1.74 ± 0.05
CVNEH	31:26:05	60:07:45	4.81 ± 0.10
West Neh			
NY-1	No GPS location		No data
4	No GPS location		27.5 ± 0.5

Uncertainties are 2 sigma. Details of the analytical procedure are given in Section 3.1. Tabulated analytical data, age and K/Ca spectra and inverse isochron plots for these samples are provided in Appendix. The samples have been divided by geographic location into those close to the Nayband fault, the East Neh fault and the West Neh fault. Unless otherwise stated, sample locations were determined with hand-held GPS and are quoted in degrees:minutes:seconds.

Each of the seven dated samples yielded results that are readily interpretable. The volcanic rocks range in age from 27.5 ± 0.5 Ma to 1.60 ± 0.15 Ma (Table 1). The majority of samples yielded flat spectra with correspondingly high-precision age determinations (samples 2, 3, AvNEH, BvNEH and CvNEH). Sample 1 produced a flat spectrum, but the very low radiogenic yields reduce the precision of age determination. The least precise date is obtained for sample 4. It is, however, clearly much older than the other samples. Sample NY-1 did not yield a reliable age. The ages, and their implications for the tectonics of the region, are discussed in Section 4.

3.2 XRF and ICP-MS measurements of elemental concentrations

The eight samples were prepared initially by grinding in an agate mill at the University of Cambridge. Whole-rock element concentrations were then determined from the powders using facilities at Leicester University. Major element data were obtained on fusion beads by X-ray fluorescence analysis using a Philips PW1400 wavelength dispersive X-ray fluoresence (XRF) spectrometer (PANalytical, Almelo, the Netherlands). Analyses were run with reference materials BH-1, MRG-1 and WS-1. Total loss on ignition (LOI) was measured on powders that had been pre-dried at 120°C for at least 12 hrs. The powders were ignited at 950°C in air for 1 hr, before cooling and reweighing. Selected trace element concentrations were also measured from the powder pellets by XRF at the University of Leicester. Calibrations were set using several reference materials (JGB-1, JP-1, W-1, BOB-1, JB-2 and BE-N).

Rare earth elements (REE) were pre-concentrated using ion exchange columns; these solutions were then analysed on a JY-Ultima-2 inductively coupled optical emission spectrometer (ICP-MS) (Horiba Jobin Yuon, Edison, NJ, USA) at the University of Leicester, UK. Calibration was carried out using internal and international geochemical reference material. Details of analytical procedures are given in Harvey *et al*. (1996). Data for the XRF and ICP-MS analyses are given in Table 3. Analyses of reference material JA-1 are reported in Table 4.

4 CONSTRAINTS ON FAULT SLIP

The eight volcanic rocks analysed in this study were chosen due to their proximity to the Nayband, West Neh, and East Neh N–S right-lateral active fault systems of eastern Iran (Fig. 1). As shown below, several of the lava flows appear to have originated at fissures or localized centres along the fault trace. The rocks have then been displaced right-laterally by continued fault movement. In this section, we use the $^{40}Ar/^{39}Ar$ ages shown in Table 2 to constrain the averaged rates of slip across the strike-slip faults in eastern Iran (Table 1).

4.1 West of the Dasht-e Lut: the Nayband fault

The Nayband fault on the western margin of the Dasht-e Lut desert is one of the longest continuous strike-slip faults in Iran (Fig. 1) and shows numerous signs of activity in the Holocene and Late Quaternary (e.g. Wellman 1966). No instrumental epicentres are recorded on the Nayband fault, and no historical seismicity is recorded (though the absence of historical seismicity may be a function of the arid desert surroundings, e.g. Ambraseys & Melville 1982). However, given its length of ∼600 km, the Nayband fault may have the

Table 3. Major (as percentages) and trace element (as parts per million) concentrations determined for the eight volcanic rock samples (see text for full details of the methods).

Sample	1	2	3	BVNEH	AVNEH	CVNEH	NY-1	4
XRF								
SiO_2	52.11	50.65	50.93	53.06	48.80	52.77	62.19	60.99
TiO_2	2.02	2.43	2.43	1.87	2.40	1.89	0.93	1.30
Al_2O_3	15.46	15.24	15.37	14.84	14.83	14.84	16.19	17.21
Fe_2O_3	8.08	9.33	9.35	8.30	9.67	7.84	5.80	5.66
MnO	0.112	0.128	0.123	0.126	0.132	0.112	0.080	0.089
MgO	4.68	5.26	5.33	5.00	5.06	4.97	1.97	1.71
CaO	8.32	8.62	8.55	9.16	10.42	8.82	4.26	4.93
Na_2O	5.29	4.98	5.05	4.90	4.80	4.86	4.44	4.54
K_2O	1.409	1.326	1.413	1.535	1.500	1.485	2.892	2.552
P_2O_5	1.138	1.135	1.142	1.081	1.289	1.003	0.300	0.434
LOI	1.08	1.33	0.54	0.69	1.59	1.32	1.53	1.40
Total	99.70	100.43	100.23	100.55	100.50	99.94	100.58	100.81
Mo	1.0	1.3	0.5	1.1	0.9	1.3	1.9	2.6
Nb	34.9	39.7	39.3	32.7	41.6	32.0	21.6	18.7
Sr	1513.9	1340.9	1389.0	1479.8	1462.1	6192.3	374.9	759.6
Rb	21.7	22.7	20.5	27.3	28.2	33.0	94.7	95.6
Zr	266.9	279.8	270.8	234.7	276.1	260.2	309.1	232.5
Y	21.4	25.4	24.7	23.4	26.1	18.9	34.3	26.1
U	−0.2	−0.7	−0.2	1.2	1.4	−0.1	2.4	2.4
Th	9.0	6.1	7.1	9.8	5.3	10.5	11.8	19.0
Pb	5.0	6.0	5.4	8.3	6.7	9.2	9.6	15.4
Ga	21.0	21.7	21.8	20.0	20.9	21.3	20.3	18.7
Zn	118.1	131.4	128.0	117.1	120.7	113.8	66.2	58.5
Cu	46.4	50.4	50.2	43.6	51.8	71.0	11.4	9.1
Ni	38.2	41.3	40.7	45.4	37.6	69.1	6.5	1.0
Co	28.7	34.0	33.0	29.1	34.6	31.0	16.3	16.2
Sc	20.8	19.2	20.5	21.0	20.5	19.6	17.2	12.8
Ba	517.4	403.9	398.2	425.3	396.9	444.8	505.2	514.5
V	152.9	202.8	222.0	184.8	214.5	189.2	95.2	94.5
Cr	137.0	82.7	149.4	94.3	138.4	200.7	109.6	13.2
Cs	1.2	0.1	−2.3	4.1	−2.6	0.0	6.9	3.9
ICP-MS								
La	47.31	40.48	43.01	45.86	39.8	45.69	30.23	29.08
Ce	92.79	84.52	92.66	100.09	83.82	90.76	59.72	55.61
Pr	24.1	21.8	21.72	22.88	21.8	23.23	13.42	14.09
Nd	43.45	46.09	49.33	50.98	41.93	43.81	27.1	23.66
Sm	8.76	9.8	10.67	10.74	8.54	8.96	6.5	5.54
Eu	2.1	2.43	2.71	2.68	2.2	2.18	1.38	1.39
Gd	5.25	6.37	6.99	7.01	5.83	5.77	5.14	4.36
Dy	3.36	4.12	4.56	4.56	3.84	3.67	4.94	3.96
Er	1.39	1.71	1.96	1.95	1.69	1.66	3.03	2.31
Yb	1	1.22	1.5	1.45	1.14	1.26	2.95	2.2
Lu	0.18	0.34	0.19	0.17	0.14	0.15	0.44	0.32

potential to generate magnitude 8 earthquakes (Berberian & Yeats 1999).

Fig. 2(a) is a LANDSAT image of part of the Nayband fault. Alkali basaltic lavas have flowed away from a line of eruptive cones along the fault trace. The largest concentration of lava has flowed SSE from the eruptive centres to form the Gandom Berian plateau. The eruptive centres are situated close to a left-step, pull-apart basin (∼5 km wide and 10 km long) in the Nayband fault trace. Localized extension within the pull-apart basin may have influenced the location of the volcanism (e.g. Camp & Griffis 1982).

Two samples of the Gandom Berian alkali basalts were dated by Conrad *et al*. (1981) at 2.08 ± 0.07 Ma and 2.05 ± 0.0.4 Ma using the K-Ar method. Kluyver *et al.* (1983) provide a petrographic description of the alkali basalts and XRF analyses of two samples. However, sample locations within the flows are not given by either Conrad *et al*. (1981) or Kluyver *et al.* (1983).

Walker & Jackson (2002) noted from the alignment of eruptive cones along the active trace of the Nayband fault (e.g. Figs. 2 and 3) that the Gandom Berian basalts must postdate the initiation of the Nayband fault. They further noted that the course of the Rud-e-Shur river, which flows southeastwards from mountainous regions west of the Nayband fault to drain into the Dasht-e Lut, and which also appears to be displaced by 3.2 km across the Nayband fault, is influenced by the southern margin of the basalt flow and will therefore postdate the emplacement of the volcanic rocks (Fig. 2). Walker & Jackson (2002) also noted an apparent right-lateral displacement of the northern margin of the basalt by a maximum of 3.2 km across the fault (Fig. 3). Using Conrad *et al.*'s (1981) K-Ar ages of ∼2 Ma, Walker & Jackson (2002) derived a right-lateral slip rate across the Nayband fault of ∼1.5 mm yr^{-1}.

We obtain new $^{40}Ar/^{39}Ar$ ages for three additional samples of the Gandom Berian basalts (samples 1, 2 and 3 in Table 1 and Fig. 2a)

Table 4. Elemental composition analyses of reference materials run with the eight volcanic rock samples.

Standard	BH-1	MRG-1	WS-1			
SiO_2	66.40	39.24	50.98			
TiO_2	0.41	3.79	2.49			
Al_2O_3	13.87	8.19	13.71			
Fe_2O_3	5.67	17.82	13.49			
MnO	0.12	0.17	0.18			
MgO	2.57	13.96	5.36			
CaO	3.31	14.62	8.62			
Na_2O	3.66	0.77	3.13			
K_2O	0.87	0.2	1.39			
P_2O_5	0.06	0.06	0.31			
LOI	2.52	1.03	0.63			
Total	99.48	99.86	100.28			
Standard	JGB-1	JP-1	W-1	BOB-1	JB-2	BE-N
Mo	1.7	0.1	1.4	1.4	0.7	2.4
Nb	3.1	1.8	8.0	5.3	0.3	106.6
Sr	329.3	0.9	190.9	188.8	176.4	1369.1
Rb	7.4	-0.7	23.1	6.0	7.8	49.4
Zr	32.9	7.5	98.6	102.8	52.2	269.3
Y	10.4	−0.4	24.3	28.2	25.5	30.1
U	0.7	0.0	0.3	1.3	2.5	2.5
Th	1.9	−0.3	3.8	0.1	−1.0	11.7
Pb	−0.9	−1.3	9.4	3.3	4.3	5.0
Ga	18.6	1.4	18.0	14.9	17.3	17.1
Zn	110.9	48.8	89.5	62.1	107.3	123.0
Cu	81.5	7.5	109.8	55.9	221.4	81.8
Ni	25.0	2447.7	73.3	102.0	13.2	273.4
Co	59.7	66.0	43.5	41.1	49.7	56.7
Sc	36.4	6.1	32.6	35.4	53.2	28.7
Ba	71.8	12.5	165.3	42.3	230.3	1009.7
V	634.4	27.6	240.2	208.0	558.2	242.0
Cr	16.1	2879.4	104.3	261.6	24.7	383.6
Cs	1.7	1.3	−4.5	1.0	1.0	0.0
Standard	JA-1 (run 1)	JA-1 (run 2)				
La	3.39	4.10				
Ce	7.03	9.48				
Pr	2.34	2.89				
Nd	7.89	9.33				
Sm	2.61	3.26				
Eu	0.84	1.02				
Gd	2.95	3.77				
Dy	3.22	4.18				
Er	2.07	2.74				
Yb	2.04	2.35				
Lu	0.31	0.40				

to further constrain the averaged slip rate across the Nayband fault. The $^{40}Ar/^{39}Ar$ technique is considered to be more robust than the K-Ar method, which is prone to the escape of radiogenic argon from minerals due to thermally activated diffusion (see Renne 2000 for a full discussion). We were also careful to obtain samples from close to both the northern and the southern margins of the lavas to test for variations in age between different parts of the flow. Samples 1 and 2, taken from close to the two main eruptive centres, are dated at 2.60 ± 0.20 Ma and 2.20 ± 0.05 Ma, respectively. Sample 3, taken from the very southern end of the flow, is dated at 2.25 ± 0.06 Ma, which is within error of the sample 2 age. The three $^{40}Ar/^{39}Ar$ ages suggest that volcanism started at least 2.6 Ma at the northernmost volcanic centre, but that the largest outpourings of lava occurred at ∼2.2 Ma. This later period of volcanism probably originated from the southern end of the two eruptive centres and formed the Gandom Berian plateau.

In our analysis of satellite imagery of the Gandum Berian region, we find that the actual offset of the margins of the basalt flows is difficult to determine with certainty. At the northern margin, the measurements of displacement are complicated by a pull-apart basin filled with lake-bed deposits, which obscures the edge of the volcanic rocks. We might also expect a northward decrease in the slip rate on approaching the pull-apart basin, as slip is transferred from the southern to the northern fault strands. Several NE–SW normal faults do cut the top surface of the basalts (Figs. 2 and 3), but the displacement across these faults is minor (less than 50 m). Although the maximum displacement across the northern margin of the basalts is 3.2 km, the trace of the southern fault strand appears

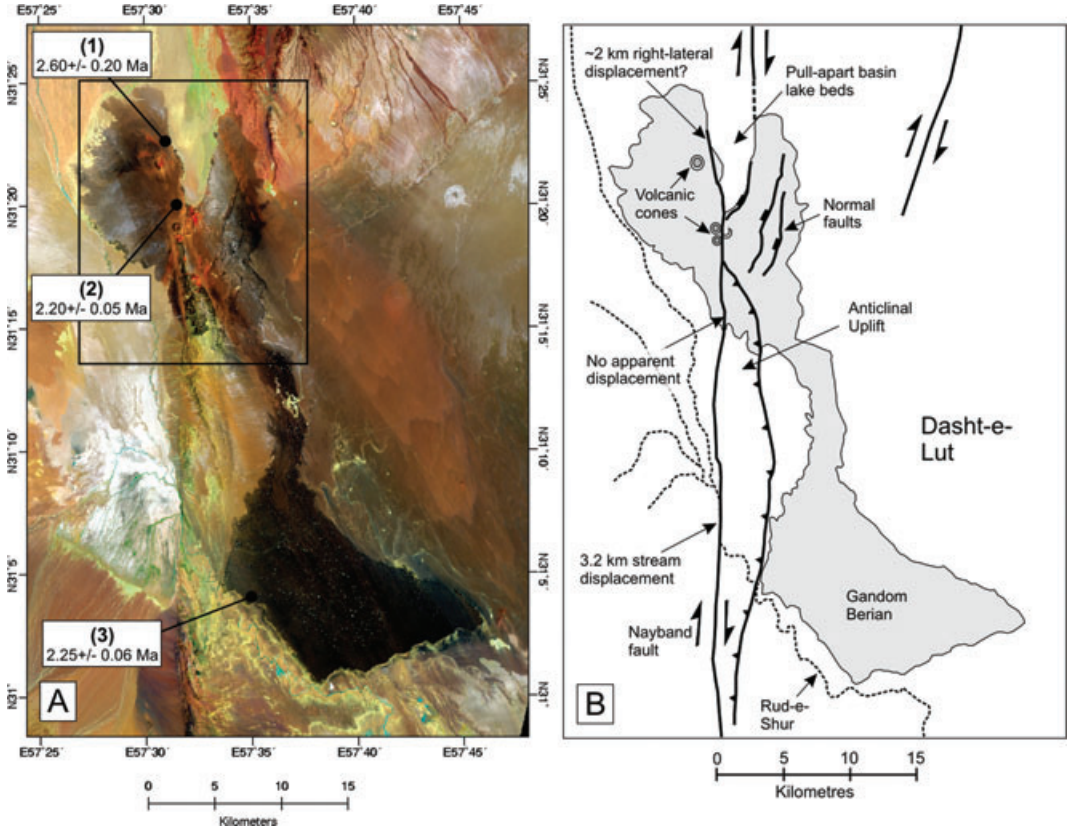

Figure 2. (a) LANDSAT TM+ scene (path-row 160–38, bands 741 displayed as red, green and blue) of the Nayband fault around the Gandum Berian alkali basalt. Sample locations and Ar-Ar ages are shown. The box marks the region represented in Fig. 3. (b) Map of the outcrops of alkali basalt (in grey) and major structural features covered by (a). The Rud-e-Shur river, whose course is diverted around the southern margin of the alkali basalts, is displaced right-laterally by 3.2 km as it crosses the Nayband fault. The across-fault displacement of the volcanics themselves is difficult to quantify due to uplift and enhanced erosion at the southern margin and burial of the flow margins by lake-bed sediments at the northern margin.

to die out at ∼31°22′N, and therefore the true displacement across the northern margin of the flow is not likely to be greater than ∼2 km (the distance between the end of the fault and the most northerly exposure of basalt on the eastern side of the fault; Fig. 3), and may be less than 2 km.

The displacement of the southern margin of the basalt would give a more reliable estimate of fault slip as this margin is not close to the pull-apart basin. Unfortunately, uplift and folding east of the Nayband fault have led to erosion and destruction of the original margin of the flow on the eastern side of the fault. Oxidized scoria, which is dark orange in the LANDSAT image, is localized at the eruptive centres on the western side of the fault (Fig. 3). Restoration of 3–4 km of right-lateral slip aligns the volcanic centres with two distinct areas of oxidation on the eastern side of the fault. Although this restoration is not certain, it does agree with the ∼3.2 km right-lateral displacement measured across the Rud-e-Shur river along the southern margin of the Gandum Berian basalts (see fig. 15 of Walker & Jackson 2002 for a detailed reconstruction of the Rud-e-Shur river displacement).

Although the exact displacement of the Gandum Berian basalts is hard to gauge with certainty, we have three slip indicators (the northern margin of the basalts, the apparent displacement of the Rud-e-Shur river course and the alignment of regions of oxidation with the eruptive cones) that place the total displacement at 2–4 km. With between 2 km and 4 km of right-lateral displacement of the volcanic rocks, the revised age of 2.15–2.31 Ma (see Table 2) for the major part of the Gandom Berian basalts provides a slip-rate estimate in the range of 0.9–1.9 mm yr^{-1} (1.4 ± 0.5 mm yr^{-1}, range is given to the nearest 0.1 mm yr^{-1}). This new estimate agrees with the 1.5 mm yr^{-1} slip rate on the Nayband fault estimated by Walker & Jackson (2002). The value of 1.4 ± 0.5 mm yr^{-1} is only a small proportion of the ∼16 mm yr^{-1} rate of right-lateral shear measured by the GPS across eastern Iran (Vernant *et al.* 2004).

4.2 East of the Dasht-e Lut: the Neh faults and Sistan Suture Zone

In this section, we look at volcanic rocks associated with a zone of active right-lateral strike-slip faulting along the eastern margin of the Dasht-e Lut in the Sistan Suture Zone (Fig. 1). The Sistan Suture Zone is a deformed accretionary prism that was emplaced during the destruction (∼89–55 Ma) of a narrow arm of the Neo-Tethys ocean (Freund 1970; Camp & Griffis 1981; Tirrul *et al.* 1983). In central parts of the N–S Suture Zone, at a latitude of ∼30.5°N, three parallel N–S right-lateral faults (the West Neh, East Neh and Zahedan faults) accommodate present-day right-lateral shear across the region (Fig. 1). Our samples are taken from outcrops close to the East and West Neh faults.

4.2.1 The East Neh fault

The locations and $^{40}Ar/^{39}Ar$ ages of the three samples AvNEH, BvNEH and CvNEH are shown on Fig. 4, in which the low-relief

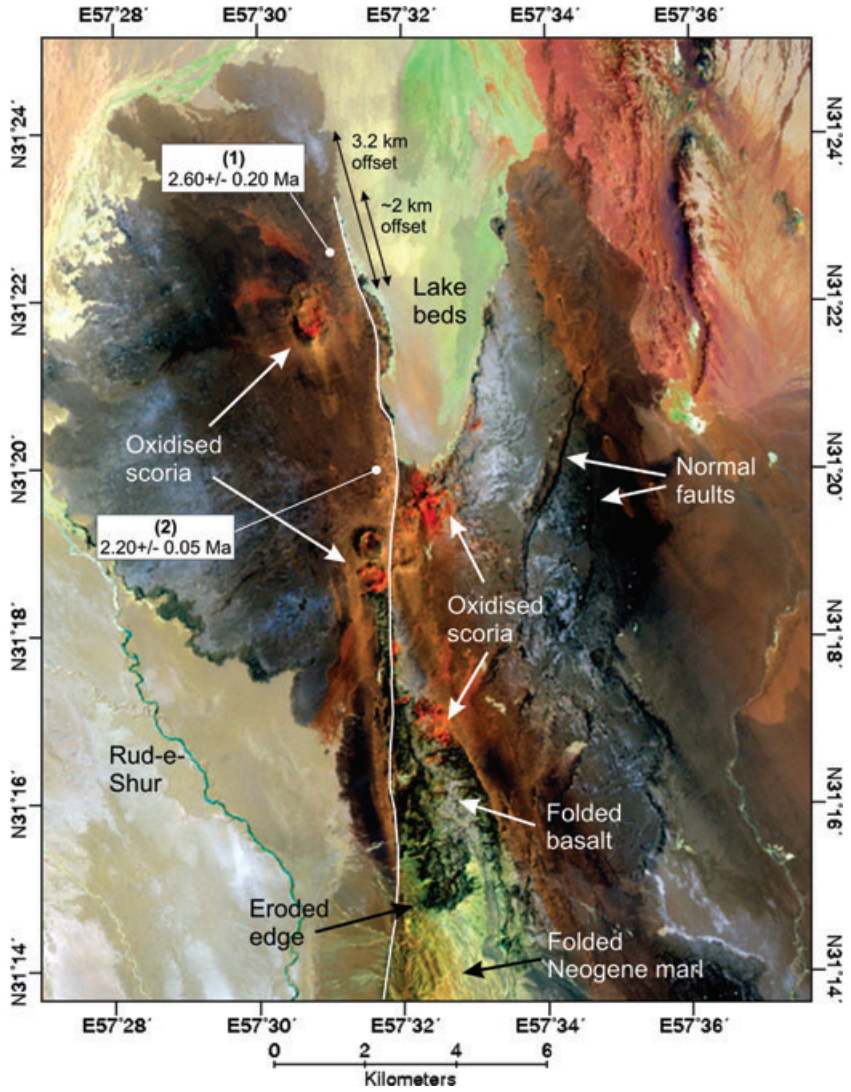

Figure 3. (a) LANDSAT TM+ scene (RGB 741) of volcanic cones at a pull-apart on the Nayband fault (see Fig. 2 for location). Several northeast–southwest trending normal fault scarps cut the surface of the flow. A segment of the Nayband fault (white line) dies out in the northern part of the image, to be replaced further north by another strand along the eastern margin of the lake beds. As such, we might not expect reconstructions of the northern margin of the flow to be reliable indicators of the overall slip rate on the Nayband fault. Displacement of the southern margin of the flow has been obliterated by enhanced erosion caused by anticlinal folding and uplift. Alignment of volcanic cones on the west side of the fault with zones of oxidation on the eastern side implies ∼3–4 km of right-lateral slip.

outcrops of alkali basalt appear as rusty or red-coloured areas. No eruptive centres are preserved, but from the shape of the outcrops, at least some of the lavas may have formed fissure eruptions along the East Neh fault trace (Camp & Griffis 1981; Fig. 4). Camp & Griffis (1981) obtained K-Ar dates of 3.8 ± 0.2 Ma, 5.7 ± 0.3 Ma and 7.3 ± 0.5 Ma for three samples of alkali basalt from the approximate area of Fig. 4(a). Unfortunately, they do not record from which of the many basalt outcrops they obtained their samples. The age range of 3.8–7.3 Ma agrees with the published geological map (GSI 1990), which marks all outcrops as Pliocene in age.

We cannot make a definite correlation of any two outcrops of lava across the fault as we have no evidence that they have originated from the same localized volcanic centre. We can, however, define rough estimates of the slip rate using the displacement of geomorphic features that postdate the basalts.

Eastward-flowing drainage channels close to sample CvNEH are offset right-laterally by ∼1 km and 5 km at the fault (Fig. 4). Further south, at the locations of samples AvNEH and BvNEH, the outcrops of lava appear to be the eroded remnants of larger original bodies, which have been cut through by rivers. The lava flows hence pre-date the river incision. In Fig. 4(c), we have labelled the parts of eastward-flowing rivers upstream from the East Neh fault from A to E. Only three streams (X, Y and Z) are present on the downstream side of the fault, though streams Y and Z are fed by several gorges that converge immediately to the east of the fault trace. The displacement of stream C (on the western side of the fault) to stream X (on the eastern side) is shown in Fig. 4(d). Stream C is, at present, displaced right-laterally by ∼1 km at the fault. The original channel of stream C is, however, defined by a linear, ENE-trending margin to bedrock incision. This ENE-trending channel is consistent with the courses of adjacent streams (A to F) on the western side of the fault and also with the ENE to eastward trend of stream X on the eastern side of the fault. A right-lateral slip on the East Neh fault has caused the course of stream C to be deflected southwards to its

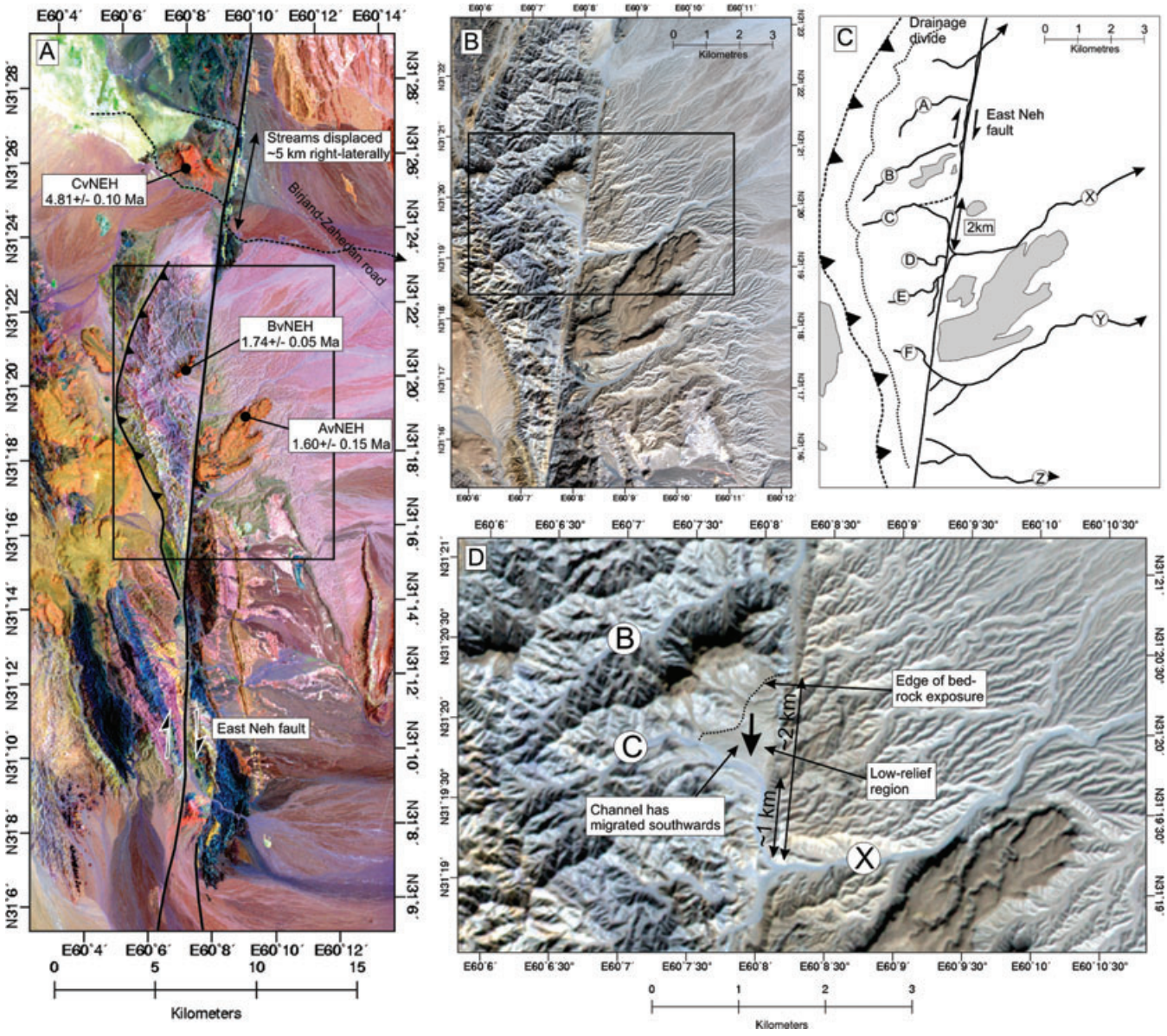

Figure 4. (a) LANDSAT TM+ scene (path-row 158–38, RGB 741) of the East Neh fault (black line) with the locations and Ar-Ar ages of samples AvNEH, BvNEH and CvNEH. CvNEH is situated close to streams that are displaced right-laterally by ∼5 km across the fault (streams marked by dotted black lines). (b) ASTER image (RGB 3n21) of the AvNEH and BvNEH sample locations. The alkali basalt outcrops are incised by an eastward-flowing drainage network and are likely to be remnants of an originally larger body of lava. The incision of drainage into lavas and underlying alluvial gravels appears to result from uplift and eastward tilting above an east-dipping thrust (inferred from the satellite imagery). Widespread incision through gravels does not occur to the west of the inferred thrust fault. (c) Sketch of (b) showing the major drainage channels and outlining the extent of alkali basalt outcrops. A minimum of 2 km of right-lateral slip is shown by restoration of C to X. This 2 km of slip does not restore the other streams to linear courses, and so we suspect that the total slip since incision of the lavas by the eastward-flowing drainage is >2 km. (d) ASTER image showing the displacement between streams C and X (see (b) for location). At present, stream X is displaced by ∼1 km at the fault. An older ENE-trending course of stream C is defined by a linear margin of bedrock exposure (marked by a dotted line). With continued strike-slip movement, stream C has migrated southwards to form a small, low-relief plain between its original and present-day channel locations.

present location, leaving a triangular, low-relief region between the original and present channel locations (Fig. 4d). The right-lateral displacement of the original course of stream C to stream X is measured at ∼2 km, which places a lower bound on the amount of fault movement since the emplacement of the lavas. However, the restoration of 2 km of slip does not produce a satisfactory alignment of drainage for streams A, B and D. In particular, streams A and B do not have an outlet, and gorge Z has no catchment. We were unable to restore all the rivers to linear courses across the fault with any given amount of slip. This is perhaps not surprising, as each of the eastward-flowing river systems might have originated at different times. It therefore appears that the magnitude of total slip since emplacement of the lavas, although unknown, is at least 2 km, and very probably more.

The $^{40}Ar/^{39}Ar$ ages are shown in Table 1 and Fig. 4(a). Sample CvNEH, located towards the north of Fig. 5, gives an age of 4.81 ± 0.10 Ma, which is well within the age range given by Camp & Griffis (1981). However, the $^{40}Ar/^{39}Ar$ ages of 1.60 ± 0.15 Ma for

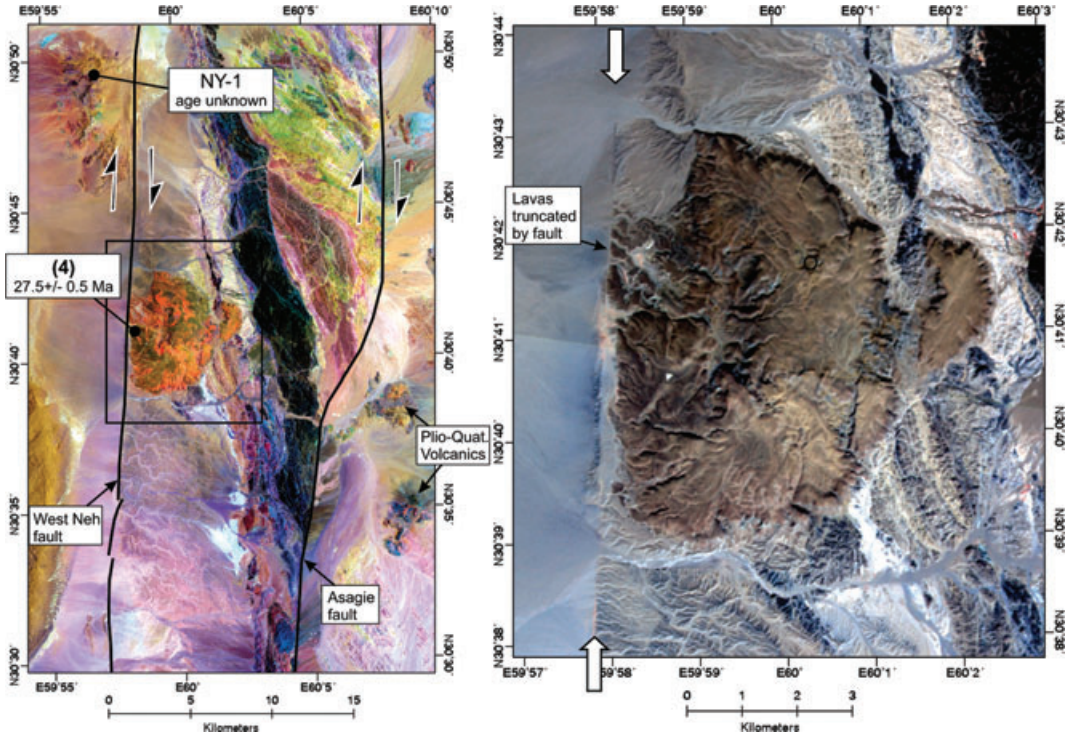

Figure 5. (a) LANDSAT TM image (path-row 158–39, RGB 741) of the West Neh and Asagie faults (marked by black lines). North of the image, the Asagie fault steps to the west and becomes the East Neh fault (Fig. 4). The approximate NY-1 and (4) sample locations are given. (b) A close-up ASTER image (RGB 3n, 2, 1) of the andesite flow situated on the West Neh fault (see box in (a) for location). The lava is truncated by the fault at its western edge. However, the outcrop pattern suggests that the volcanic centre was situated to the east of the fault trace. As such, the close spatial correlation between faulting and volcanism could be coincidental, and no firm conclusions can be drawn on the age of faulting.

sample AvNEh and 1.74 ± 0.05 Ma for BvNEH are much younger than previously thought. As the East Neh fault must have moved at least 2 km since eruption of the lavas at ∼1.7 Ma, a lower bound of 1.2 mm yr^{-1} is placed on the slip rate. However, it is likely that the fault has moved substantially more than 2 km since this time, in which case, the slip rate will be higher.

4.2.2 The West Neh fault

LANDSAT satellite imagery of the central part of the West Neh fault is shown in Fig. 5. A total cumulative displacement of ∼10 km on the West Neh fault is measured by Walker & Jackson (2004) from the displacement of steeply dipping ophiolitic mélange units (situated further north than the region shown in Fig. 5). Two samples (number 4 and NY-1) were collected from outcrops of volcanic rock located close to the fault. Sample 4 was taken from the margin of an almost circular outcrop of andesitic volcanic rock truncated at its western side by the West Neh fault. NY-1 was taken from a highly eroded andesitic outcrop situated slightly to the west of the West Neh fault (Fig. 5).

The $^{40}Ar/^{39}Ar$ age of 27.5 ± 0.5 Ma determined for sample 4 (Table 1) shows the lava to be much older than the Plio-Quaternary age assigned on the geological map (GSI 1991). We were unable to determine an age for NY-1, although it is presumably also relatively old as the outcrops are rather eroded in comparison to those near the Nayband and East Neh faults. Although samples 4 and NY-1 are of similar composition (see Section 5), we cannot make a correlation of the andesitic rocks across the fault and so cannot provide a slip-rate estimate. Both of the flows show a close spatial association with the trace of the West Neh fault (Fig. 5), but neither of them appears to have been erupted along the fault line itself. The $^{40}Ar/^{39}Ar$ age of ∼27.5 Ma for sample 4 suggests either that the volcanism pre-dates the onset of faulting or that the West Neh fault is much older than we have assumed. The spatial relationship between the volcanism and the fault are not well defined to distinguish between these two possibilities.

4.3 Rates of faulting: discussion

Our results show that, averaged over the last 2 Ma, the Nayband fault has accumulated only ∼1.5 mm yr^{-1} of the total ∼16 mm yr^{-1} rate of right-lateral shear in eastern Iran. We have also found that the East Neh fault, which is only one of several active faults in the Sistan Suture Zone, has a minimum slip rate of ∼1.2 mm yr^{-1} when averaged over the last ∼1.6–1.8 Ma. The minimum slip rate that we determine for the East Neh fault is a little lower, but not inconsistent, with the range obtained by Meyer & Le Dortz (2007) from the restoration of alluvial fans of assumed Holocene age (1.75–2.50 mm yr^{-1}).

However, the consistency between the Holocene and long-term slip-rate estimates for the East Neh fault relies on two major assumptions. First, the Holocene estimates of Meyer & Le Dortz (2007) rely on an assumed age of ∼12 Ka for the alluvial fans whose displacements they measure. Although this assumption seems reasonable, and is supported by studies elsewhere in Iran (Regard *et al.* 2005; Fattahi *et al.* 2006, 2007), the hypothesis cannot be validated until quantitative age constraints are obtained for the displaced fans. Second, displaced lava flows described in the present paper do not constrain the maximum slip rate of the East Neh fault (see

Section 4.2.1), and as such, the actual long-term slip rate could exceed the inferred 2.5 mm yr^{-1} Holocene maximum.

One aspect of the deformation in eastern Iran that is well determined is that ∼16 ± 2 mm yr^{-1} rate of N–S right-lateral shear is accommodated, at the present day, between Iran and Afghanistan (Vernant *et al.* 2004). The overall convergence between Arabia and Eurasia has been constant since ∼56 Ma (McQuarrie *et al.* 2003), and there is, therefore, no reason to suggest that the overall rate of shearing has varied substantially over the late Quaternary. The ∼16 mm yr^{-1} rate of shear is split, at present, into components on the east (Sistan Suture Zone) and the west (Nayband-Gowk-Sabzevaran system) side of the Dasht-e Lut. Less well determined, however, is the extent to which GPS (geodetic) measurements are representative of the longer term distribution of slip on faults in eastern Iran (Meyer & Le Dortz 2007).

Meyer & Le Dortz (2007) suggest that only 1.5 mm yr^{-1} rate of the total right-lateral shear is accommodated on the western margin of the Dasht-e Lut on the Sabzevaran–Gowk–Nayband fault system. The 1.5 mm yr^{-1} value comes from the Quaternary rate on the Nayband fault derived by Walker & Jackson (2002) and is refined in Section 4.1 of this paper. However, the total long-term rate of shear across the western Dasht-e Lut margin varies with latitude. It is measured at a 4.0–7.4 mm yr^{-1} rate across the Sabzevaran fault (Regard *et al.* 2005), which is substantially higher than the 1.5 mm yr^{-1} rate measured further north across the Nayband fault. The reason for this northward decrease in slip rate can be seen in Fig. 1. At its northern end, the Sabzevaran fault separates into the Gowk fault that continues northwards along the Dasht-e Lut margin (e.g. Walker & Jackson 2002), and the Rafsanjan fault, which trends northwest into central Iran (e.g. Berberian 1976; Walker 2006). At the northern end of the Gowk fault, it, in turn, separates into the Nayband, Kuh Banan and Lakar Kuh faults (the latter is not labelled on Fig. 1). The Kerman (KERM) GPS station is adjacent to the Gowk fault, and hence the rate of shear along the western Dasht-e Lut margin at the latitude of GPS station KERM is accommodated by the Gowk fault. The slip rate on the Gowk fault is not known, but will be a maximum of 4.0–7.4 mm yr^{-1} (if the Rafsanjan fault accommodates negligible slip) and ∼1.5 mm yr^{-1} (if the Kuh Banan and Lakar Kuh faults are inactive). As all the aforementioned faults show clear evidence of late Quaternary slip (e.g. Berberian 1976), it is likely that the Gowk fault slip rate is somewhere in the middle of this range.

Using the (probably unrealistic) upper end of possible slip rates for the Gowk fault of 7.4 mm yr^{-1}, and taking the 2.7–7.5 mm yr^{-1} slip rates inferred by Meyer & Le Dortz (2007) for the East and West Neh faults in the Sistan suture zone, accounts for 10.1–14.9 mm yr^{-1} of the 16 ± 2 mm yr^{-1} rate of right-lateral shear recorded between the GPS stations KERM and ZABO. If we assume, for example, a rate of 3 mm yr^{-1} on the Gowk fault (less than half the possible range), the total shear accounted for is 5.7–10.5 mm yr^{-1}. A slip rate of just a few millimetres per year is all that is required on the Zahedan fault—and other minor faults within eastern Iran—to reconcile these long-term rates with the GPS-derived rates of 16 ± 2 mm yr^{-1}. We see no reason why it is not feasible for the Zahedan (and other) faults to accommodate the shortfall.

Although it is clear that the ∼16 mm yr^{-1} rate of N–S right-lateral shear between Iran and Afghanistan is split between several fault systems both to the east and to the west of the Dasht-e Lut, the existing slip-rate data are not sufficient to determine exactly how the deformation is distributed as slip on each of the faults. Our best estimates of the distribution of shear at the latitude of the GPS stations KERM and ZABO, and assuming that the inferred estimates of Meyer & Le Dortz (2007) are correct, are that more than 2.7–7.5 mm yr^{-1} (i.e. the slip rates of the Neh faults plus the unknown contribution of the Zahedan and other minor faults) is taken up across the Sistan Suture Zone, and a value less than 4.0–7.4 mm yr^{-1} (i.e. the Sabzevaran slip rate of Regard *et al.* 2005, minus the unknown slip rate of the Rafsanjan and additional minor faults) is accommodated as slip on the Gowk fault west of the Dasht-e Lut desert. Given the extremely large uncertainties in what is known of the distribution of slip on faults around eastern Iran, it is extremely difficult to say, with our present state of knowledge, whether any discrepancy exists between the Quaternary slip-rate estimates for individual faults and the GPS-derived pattern of present-day deformation. We anticipate that further dating studies over the coming years will improve our knowledge of slip rates on the major faults of eastern Iran and will enable a more complete description of the kinematics of deformation in eastern Iran.

5 COMPOSITION AND ORIGIN OF THE VOLCANIC ROCKS

Although the main aim of this paper is to determine the slip rate of major faults in eastern Iran, our eight volcanic rock samples were collected from a remote, and little studied, part of the Arabia–Eurasia collision zone where high surface elevation, a long-wavelength free-air gravity high and a low seismic velocity anomaly in the upper mantle have been used to suggest partial delamination of the thickened lithosphere (e.g. Maggi & Priestley 2005). Recently published global maps of lithospheric thickness derived from shear wave velocities (Priestley & McKenzie 2006; McKenzie & Priestley 2008) suggest abrupt changes in lithospheric thickness between the NE and SW parts of Iran, with the latter having a lithospheric thickness of ∼260 km, and suggesting that the SW Iranian lithosphere has not delaminated. We therefore include elemental compositions of the eight samples, and also provide a brief discussion of the chemistry of the rocks, to investigate their implications for the lithosphere of Iran.

Table 2 shows elemental concentrations for all eight samples. The three Nayband samples are all hawaiites, based on their alkali and silica abundances. The East Neh samples are transitional between hawaiite and trachyandesite, whereas the West Neh samples are more evolved and fall at the more acidic end of the trachyandesite spectrum. Fig. 6 shows multi-element variation plots ('spiderdiagrams') for the eight samples, normalized to mid-ocean ridge basalt (MORB; Pearce 1982; Sun & McDonough 1989). The abundance of each element is shown as a ratio of its abundance in average N-type MORB, with increasing incompatibility towards the left. The compositions are similar to the signatures seen in ocean island basalts (OIB), with elevated abundances of the large ion lithophile elements (LILE; e.g. Sr, Ba and Rb) compared with high-field strength elements (HFSE; e.g. Zr, Y and Ti). There are small negative Nb anomalies in all individual patterns (La/Nb ∼1.0–1.6), but this may be due to crustal contamination rather than due to source region composition: there is a positive correlation between La/Nb and indicators of fractionation, such as SiO_2. The contamination sensitive ratio Rb/Nb also increases with fractionation.

As the abundances of REE are sensitive to both the amounts and the depths of melting, we invert the observed abundances, using the code of McKenzie & O'Nions (1991) and an assumed initial source of primitive mantle, to provide information on the distribution of melting with depth. The results are shown in

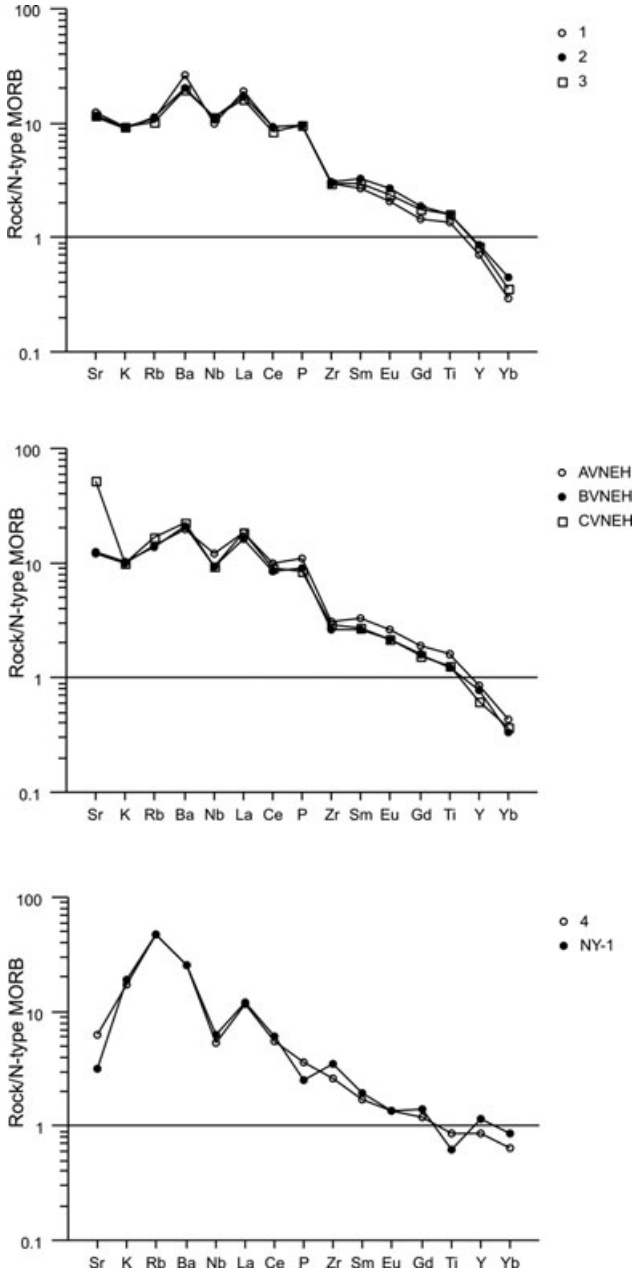

Figure 6. Multi-element variation plots ('spiderdiagrams') for the eight samples, normalized to mid-ocean ridge basalt (MORB; Pearce 1982; Sun & McDonough 1989). The abundance of each element is shown as a ratio of its abundance in average N-type MORB, with increasing incompatibility towards the left. The data are presented in Table 3. See text for further details

Fig. 7 (provided by McKenzie, personal communication, 2006). An interesting result from this analysis is that the data cannot be fitted by a single-stage melting in the garnet stability field (i.e. melting at depths >80 km). Instead, the observed concentrations require enrichment from a 0.5% melting of a peridotite source within the garnet stability field followed by melting within the spinel stability field. The melting curves in Fig. 7 are those of the source after enrichment.

The compositions of the volcanic rocks are typical of OIBs and are therefore not likely to arise from melting of mantle lithosphere. The failure to reproduce the observed geochemical data by melt generation solely in the garnet stability field therefore suggests that the lithospheric mantle beneath NE Iran is relatively thin. The presence of lithosphere with thickness <125 km is also suggested beneath NE Iran by maps of lithospheric thickness obtained from shear wave velocities (Priestley & McKenzie 2006; McKenzie & Priestley 2008). Our results are therefore consistent with lithospheric thickness maps derived from shear wave velocity.

Plio-Quaternary volcanic rocks do not occur everywhere within Iran (Fig. 1). The volcanics are widespread within eastern and central parts of the country, particularly close to active strike-slip faults (Fig. 1). The activity ceases along an NW–SE line just to the north of the Zagros (Fig. 1), consistent with no melt generation southwest of the original Arabia–Eurasia suture. The distribution of Plio-Quaternary volcanics is predominantly in areas with lithosphere thickness of <125 km (Priestley & McKenzie 2006; McKenzie & Priestley 2008).

6 CONCLUSIONS

Our rather small set of volcanic rocks from eastern Iran has provided several new and important results. Combining $^{40}Ar/^{39}Ar$ ages with displacements of the volcanic bodies across active strike-slip faults has yielded slip-rate estimates for both the Nayband ($\sim$1.5 mm yr^{-1}) and the East Neh faults (>1.2 mm yr^{-1}). These rates are some of the first quantitative data from this tectonically active, and extremely remote, part of the world. Elemental compositions of the rocks and inversion of REE concentrations also provide constraints on the lithospheric structure of eastern Iran. The analyses suggest the volcanic rocks partially originate from a probable source of asthenospheric mantle at depths of $\sim$80 km below the earth's surface. The geochemistry of the rocks is therefore indicative of a thin lithosphere beneath NE Iran and agrees with recently published maps of lithospheric thickness derived from shear wave velocities.

ACKNOWLEDGMENTS

We thank the University of Birjand for their help and for providing a grant to cover fieldwork and shipping expenses. We also thank the Geological Survey of Iran for their continued support. We thank A. Saunders for his support in making the geochemical analyses and V. Martin for her help in preparing the samples. J. MacLennan and D. McKenzie provided useful comments on an earlier draft of the manuscript. D. McKenzie also kindly applied the INVMEL code (McKenzie & O'Nions 1991) to our data. We are grateful to Bernard Guest and Bertrand Meyer for providing constructive reviews that were extremely helpful in shaping the final manuscript. RW is funded by the Royal Society. This research is supported by the NERC-funded Centre for the Observation and Modelling of Earthquakes and Tectonics (COMET).

REFERENCES

Agard, P., Omrani, J., Jolivet, L. & Mouthereau, F., 2005. Convergence history across Zagros (Iran): constraints from collisional and earlier deformation, *Int. J. Earth. Sci.,* **94,** 401–419.

Allen, M. Jackson, J. & Walker, R., 2004. Late Cenozoic reorganization of the Arabia-Eurasia collision and the comparison of short-term and long-term deformation rates, *Tectonics,* **23,** TC2008, doi: 10.1029/2003TC001530.

Allen, M.B., Walker, R., Jackson, J., Blanc, E.J-P, Talebian, M. & Ghassemi, M.R., 2006. Contrasting styles of convergence in the

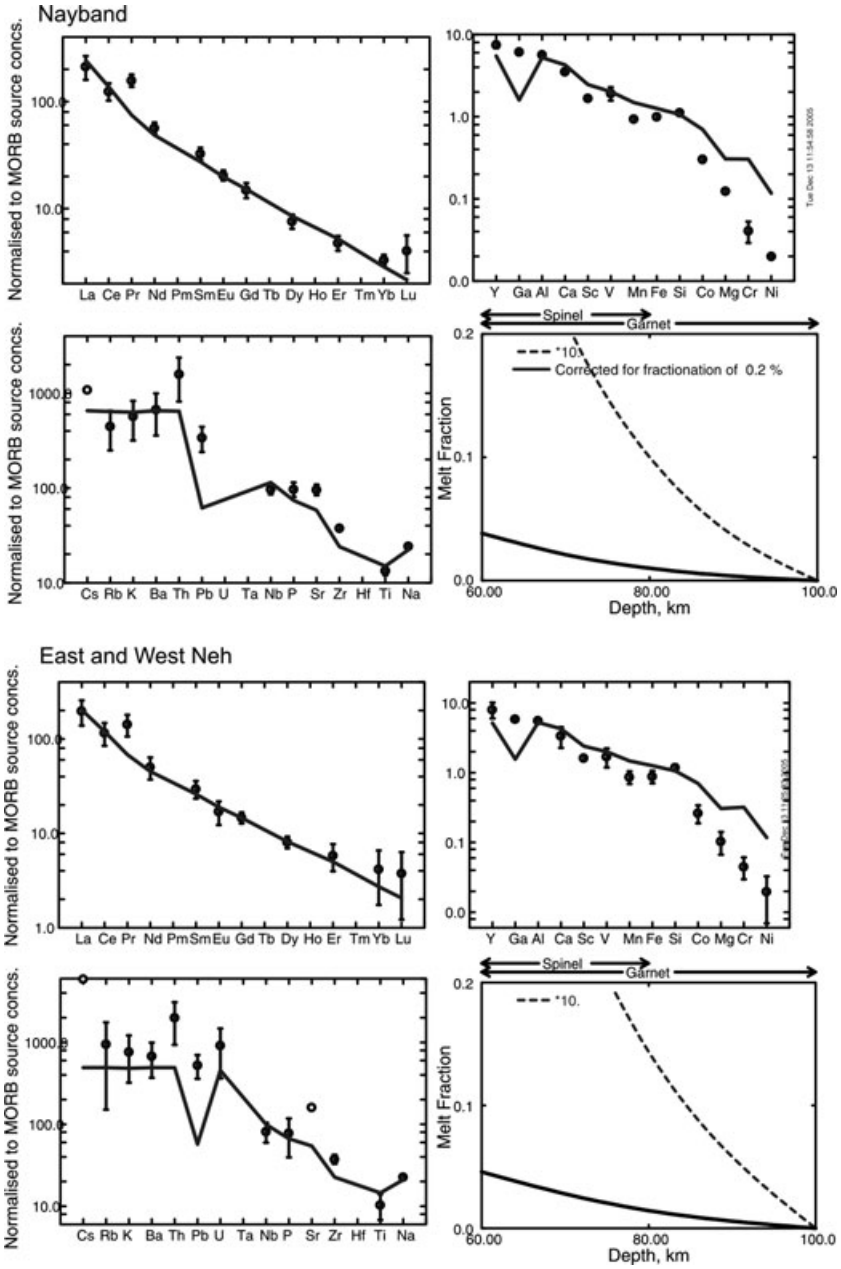

Figure 7. Inversion of REE concentrations (a subset of those in Table 3) for depths and amounts of melting using the INVMEL code of McKenzie & O'Nions (1991). The upper four panels show results for samples situated close to the Nayband fault. The lower panels show results for samples from the East Neh and West Neh faults (excluding sample 4, which had very low Mg concentration). In each set of analyses, the fourth panel shows the depth and fraction of melting which best reproduces the observed REE concentrations. The melt added to both sources was generated in the garnet stability field by extracting about 0.5% melt from a peridotite with the composition of the MORB source of McKenzie & O'Nions (1991). Three per cent of this enriching melt was added. The melting curve is that of the source after enrichment. The other three panels show the elemental concentrations predicted from the melting model (solid line) overlain on the measured elemental concentrations. The low concentrations of Co, Mg, Cr and Ni relative to the modelled concentrations probably arise from fractionation as the melt cools.

Arabia-Eurasia collision: why escape tectonics does not occur in Iran, *Geol. Soc. Am.,* Special Paper **409,** 579–589.

Almandaz, E., Pearce, J.A., Thirlwall, M.F. & Mitchell, J.G., 2000. Petrogenetic evolution of late Cenozoic, post-collision volcanism in western Anatolia, Turkey, *J. Volcanol. Geoth. Res.,* **102,** 67–95.

Ambraseys, N.N. & Melville, C.P., 1982. *A History of Persian Earthquakes*. Cambridge University Press, Cambridge, UK.

Axen, G.J., Lam, P.S., Grove, D., Stockli, D. & Hassanzadeh, J., 2001. Exhumation of the west-central Alborz mountains, Iran, Caspian subsidence, and collision-related tectonics, *Geology,* **29,** 559–562.

Bayer, R. *et al*., 2006. Active deformation in Zagros–Makran transition zone inferred from GPS measurements, *Geophys. J. Int.,* **165,** 373–381.

Berberian, M., 1976. Contribution to the seismotectonics of Iran (Part II), Report no. 39, Geological Survey of Iran.

Berberian, M. & Yeats, R.S., 1999. Patterns of historical earthquake rupture in the Iranian plateau, *Bull. Seismol. Soc. Am.,* **89,** 120–139.

Camp, V.E. & Griffis, R.J., 1981. Character, genesis and tectonic setting of igneous rocks in the Sistan suture zone, eastern Iran, *Lithos,* **3,** 221–239.

Conrad, G., Montigny, R., Thuizat, R. & Westphal, M., 1981. Tertiary and Quaternary geodynamics of southern Lut (Iran) as deduced from

palaeomagnetic, isotopic and structural data, *Tectonophysics,* **75,** T11–T17.
Copley, A. & Jackson, J., 2006. Active tectonics of the Turkish-Iranian plateau, *Tectonics,* **25,** TC6006.
Dolan, J., Bowman, D. & Sammis, C., 2007. Long-range and long-term fault interactions in Southern California, *Geology,* **35,** 855–858.
Emami, M.H., Mir Mohammad Sadeghi, M. & Omrani, S.J., 1993. Magmatic map of Iran, scale 1:1, 000, 000, Geological Survey of Iran.
Engdahl, E.R., Van Der Hilst, R. & Buland, R., 1998. Global teleseismic earthquake relocation with improved travel times and procedures for depth determination, *Bull. Seismol. Soc. Am.,* **88,** 722–743.
Fattahi, M., Walker, R., Hollingsworth, J., Bahroudi, A., Talebian, M. & Stokes, S., 2006. Holocene slip-rate on the Sabzevar thrust fault, NE Iran, determined using optically-stimulated luminescence (OSL), *Earth. Planet. Sci. Lett.,* **245,** 673–684.
Fattahi, M., Walker, R., Khatib, M.M., Dolati, A. & Bahroudi, A., 2007. Past earthquakes and slip-rate estimates on the Doruneh fault, NE Iran, *Geophys. J. Int.,* **168,** 691–709.
Freund, R., 1970. Rotation of strike-slip faults in Sistan, southeast Iran, *J. Geol.,* **78,** 188–200.
GSI, 1990. Geological Quadrangle map of Iran, 1:250, 000 scale, sheet L9/M9 (Zabol), Geological Survey of Iran.
GSI, 1991. Geological Quadrangle map of Iran, 1:250, 000 scale, sheet L10/M19 (Daryacheh-ye-Hamun), Geological Survey of Iran.
Guest, B.D.E., Stockli, D., Grove, G.J., Axen, Lam, P.S. & Hassanzadeh, J., 2006. Thermal histories from the central Alborz mountains, northern Iran: implications for the spatial and temporal distributions of deformation in northern Iran, *Geol. Soc. Am. Bull.,* **118,** 1507–1521.
Hollingsworth, J., Jackson, J., Walker, R., Gheitanchi, M.R. & Bolourchi, M.J., 2006. Strike-slip faulting, rotation, and along-strike elongation in the Kopeh Dagh mountains, NE Iran, *Geophys. J. Int.,* **166,** 1161–1177.
Jackson, J. & McKenzie, D., 1984. Active tectonics of the Alpine-Himalayan belt between western Turkey and Pakistan, *Geophys. J. Roy. Astr. Soc.,* **77,** 185–264.
Keskin, M., Pearce, J.A. & Mitchell, J.G., 1998. Volcano-stratigraphy and geochemistry of collision-related volcanism on the Erzurum-Kars Plateau, northeastern Turkey, *J. Volcanol. Geoth. Res.,* **85,** 355–404.
Kluyver, H.M., Tirrul, R., Chance, P.N., Johns, G.W. & Meixner, H.M. 1983. Explanatory text of the Naybandan Quadrangle map 1:250, 000. Geological Survey of Iran, Tehran, Geological Quadrangle, No. J8, p. 143.
Maggi, A. & Priestley, K., 2005. Surface waveform tomography of the Turkish-Iranian Plateau, *Geophys. J. Int.,* **160,** 1068–1080.
McKenzie, D. & O'Nions, R.K., 1991. Partial melt distributions from inversion of rare earth element concentrations, *J. Petrol.,* **32,** 1021–1091.
McKenzie, D. & Priestley, K., 2008. The influence of lithospheric thickness variations on continental evolution, *Lithos,* **102,** 1–11.
McQuarrie, N., Stock, J.M., Verdel, C. & Wernicke, B.P., 2003. Cenozoic evolution of Neotethys and implications for the causes of plate motions, *Geophys. Res. Lett.,* **30,** doi: 10.1029/2003GL017992.
Meyer, B. & Le Dortz, K., 2007. Strike-slip kinematics in Central and Eastern Iran: estimating fault slip-rates averaged over the Holocene, *Tectonics,* **26,** TC5009, doi:10.1029/2006TC002073.
Meyer, B., Mouthereau, F., Lacombe, O. & Agard, P., 2006. Evidence of Quaternary activity along the Deshir fault: implication for the Tertiary tectonics of Central Iran, *Geophys. J. Int.,* **164,** 192–201.
Pearce, J.A., 1982. Trace element characteristics of lavas from destructive plate margins, in *Andesites: Orogenic Andesites and Related Rocks,* pp. 525–548, ed. Thorpe, R.S., Wiley, New York.
Pearce, J.A. *et al*., 1990. Genesis of collision volcanism in Eastern Anatolia, Turkey, *J. Volcanol. Geoth. Res.,* **44,** 189–229.
Priestley, K. & McKenzie, D., 2006. The thermal structure of the lithosphere from shear wave velocities, *Earth. Planet. Sci. Lett.,* **244,** 285–301.
Regard, V. *et al*., 2005. Cumulative right-lateral fault slip-rate across the Zagros-Makran transfer zone: role of the Minab-Zendan fault system in accommodating Arabia-Eurasia convergence in SE Iran, *Geophys. J. Int.,* **162,** 177–203.
Renne, P.R., 2000. K-Ar and $^{40}Ar/^{39}Ar$ dating, in *Quaternary Geochronology: Methods and Applications,* pp. 77–100 eds. Noller, J.S., Sowers, J.M. & Lettis, W.R., AGU Reference Shelf 4, American Geophysical Union, Washington, DC.
Sun, S.S. & McDonough, W.F., 1989. Chemical and isotopic systematics of oceanic basalts: implications for mantle composition and processes, in *Magmatism in the Ocean Basins,* pp. 313–345, eds. Saunders, A.D. & Norry M.J., Geological Society of London (Special Publication 42).
Talebian, M. & Jackson, J., 2002. Offset on the Main Recent fault of NW Iran and implications for the late Cenozoic tectonics of the Arabia-Eurasia collision zone, *Geophys. J. Int.,* **150,** 422–439.
Tirrul, R., Bell, I.R., Griffis, R.J. & Camp, V.E., 1983. The Sistan suture zone of eastern Iran, *Geol. Soc. Am. Bull.,* **94,** 134–150.
Verdel, C., Wernicke, B.P., Ramezani, J., Hassanzadeh, J., Renne, P.R. & Spell, T.L., 2007. Geology and thermochronology of Tertiary Cordilleran-style metamorphic core complexes in the Saghand region of central Iran, *Geol. Soc. Am. Bull.,* **119,** 961–977.
Vernant, P. *et al*., 2004. Present-day crustal deformation and plate kinematics in the Middle East constrained by GPS measurements in Iran and northern Oman, *Geophys. J. Int.,* **157,** 381–398.
Vincent, S.J., Allen, M.B., Ismail-Zadeh, A.D., Flecker, R., Foland, K.A. & Simmons, M.D., 2005. Insights from the Talysh of Azerbaijan into the Paleogene evolution of the South Caspian region, *Bulletin of the Geological Society of America*, **117,** 1513–1533.
Walker, R. & Jackson, J., 2002. Offset and evolution of the Gowk fault, S.E. Iran: a major intra-continental strike-slip system, *J. Struct. Geol.,* **24,** 1677–1698.
Walker, R. & Jackson, J., 2004. Active tectonics and late Cenozoic strain distribution in central and eastern Iran, *Tectonics,* **23,** TC5010, doi: 10.1029/2003TC001529.
Walker, R., Jackson, J. & Baker, C., 2004. Active faulting and seismicity of the Dasht-e-Bayaz region, eastern Iran, *Geophys. J. Int.,* **157,** 265–282.
Wellman, H.W., 1966. Active wrench faults of Iran, Afghanistan and Pakistan, *Geol. Rundsch.,* **18,** 217–234.

APPENDIX A

Tabulated analytical data, age and K/Ca spectra and inverse isochron plots for the samples in Table 2.

Sample:		SB53-5	JJ-1 WR		$J = 0.0002776$					
T	*t*	40(mol)	40/39	38/39	37/39	36/39	K/Ca	$\sum {}^{39}$Ar	^{40}Ar*	Age (Ma)
560	12	$8.2e^{-14}$	198.9310	$1.7e^{-3}$	1.2032	0.6531	0.41	0.06243	0.030	3.0 ± 0.5
600	12	$5.2e^{-14}$	150.7805	$0.0e^{+0}$	1.2432	0.4941	0.39	0.11500	0.032	2.4 ± 0.4
650	12	$6.6e^{-14}$	104.0627	$3.2e^{-3}$	1.1961	0.3355	0.41	0.21111	0.047	2.5 ± 0.2
700	12	$6.6e^{-14}$	75.8274	$0.0e^{+0}$	1.0295	0.2382	0.48	0.34365	0.072	2.7 ± 0.2
750	12	$5.8e^{-14}$	65.8674	$0.0e^{+0}$	0.8571	0.2056	0.57	0.47677	0.078	2.6 ± 0.1
800	12	$5.3e^{-14}$	69.6923	$0.0e^{+0}$	0.9158	0.2185	0.54	0.59296	0.073	2.6 ± 0.2
860	12	$5.6e^{-14}$	96.0579	$8.5e^{-4}$	1.2333	0.3070	0.40	0.68130	0.056	2.7 ± 0.2
920	12	$9.7e^{-14}$	190.8633	$0.0e^{+0}$	1.5582	0.6273	0.31	0.75827	0.029	2.8 ± 0.4
990	12	$1.1e^{-13}$	207.2829	$4.9e^{-3}$	1.8722	0.6852	0.26	0.83751	0.023	2.4 ± 0.4
1060	12	$8.1e^{-14}$	185.7267	$0.0e^{+0}$	2.3057	0.6190	0.21	0.90328	0.015	1.4 ± 0.4
1160	12	$2.1e^{-13}$	328.5274	$5.7e^{-3}$	2.6877	1.0944	0.18	1.00000	0.016	2.6 ± 0.7

Total fusion age (TFA) $= 2.53 \pm 0.10$ Ma (including *J*)
Weighted mean plateau age (WMPA) $= 2.59 \pm 0.07$ Ma (including *J*)
Inverse isochron age $= 2.65 \pm 0.12$ Ma. (MSWD $= 0.62$; ^{40}Ar/^{36}Ar $= 295.1 \pm 0.6$)
Steps used: 600, 650, 700, 750, 800, 860, 920, 990 (2–9/11 or 78% $\sum {}^{39}$Ar
t = dwell time in minutes.
40(mol) = moles corrected for blank and reactor-produced 40.
Ratios are corrected for blanks, decay and interference.
$\sum^{39}$Ar is cumulative, ^{40}Ar* = rad fraction.

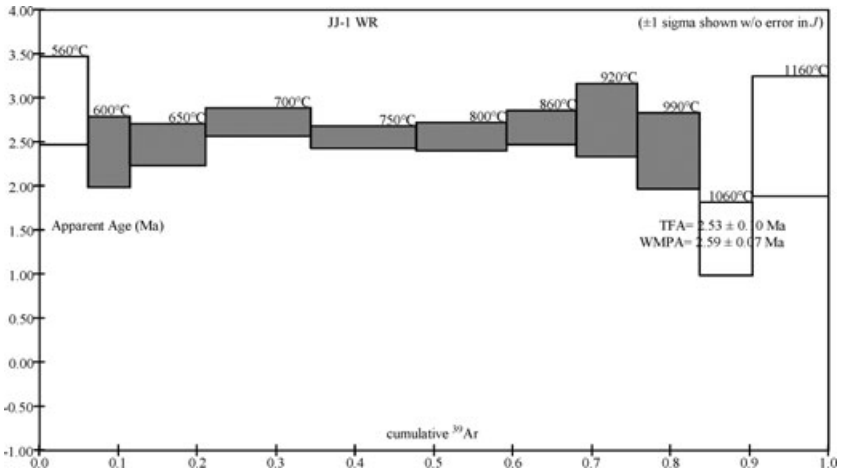

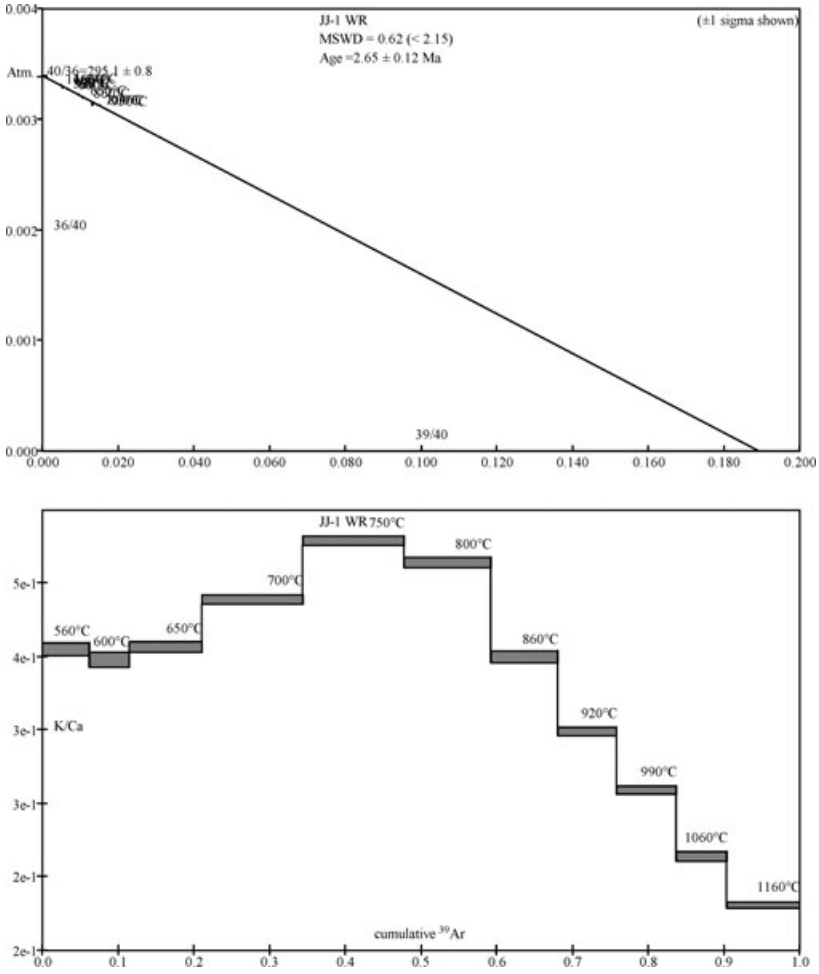

Sample:		SB53-9	JJ-2 WR		$J = 0.0002730$					
T	*t*	40(mol)	40/39	38/39	37/39	36/39	K/Ca	$\sum {}^{39}$Ar	^{40}Ar*	Age (Ma)
560	12	$3.8e^{-14}$	66.2911	$5.1e^{-3}$	1.3490	0.2156	0.36	0.04504	0.039	1.3 ± 0.2
600	12	$2.6e^{-14}$	43.9183	$6.0e^{-3}$	1.3731	0.1393	0.36	0.09086	0.063	1.4 ± 0.1
650	12	$2.9e^{-14}$	29.4692	$2.1e^{-3}$	1.2679	0.0856	0.39	0.16814	0.142	2.1 ± 0.1
700	12	$2.9e^{-14}$	20.9443	$0.0e^{+0}$	1.1183	0.0549	0.44	0.27720	0.226	2.3 ± 0.1
760	12	$3.0e^{-14}$	15.6658	$0.0e^{+0}$	0.9202	0.0376	0.53	0.43017	0.290	2.2 ± 0.0
820	12	$2.4e^{-14}$	12.9063	$0.0e^{+0}$	0.8322	0.0287	0.59	0.57824	0.343	2.2 ± 0.0
890	12	$1.9e^{-14}$	13.6256	$0.0e^{+0}$	0.9537	0.0312	0.51	0.68934	0.322	2.2 ± 0.0
980	12	$2.6e^{-14}$	17.0412	$5.4e^{-4}$	1.2146	0.0426	0.40	0.80718	0.262	2.2 ± 0.0
1060	12	$2.0e^{-14}$	18.8942	$0.0e^{+0}$	1.8437	0.0498	0.27	0.89032	0.221	2.1 ± 0.0
1160	12	$4.2e^{-14}$	29.8278	$0.0e^{+0}$	2.6301	0.0877	0.19	1.00000	0.132	1.9 ± 0.1

Total fusion age (TFA) = 2.08 ± 0.02 Ma (including *J*)
Weighted mean plateau age (WMPA) = 2.19 ± 0.02 Ma (including *J*)
Inverse isochron age = 2.09 ± 0.11 Ma. (MSWD = 0.93; ^{40}Ar/^{36}Ar = 301.9 ± 6.1)
Steps used: 760, 820, 890, 980 (5–8/10 or 53% $\sum {}^{39}$Ar)
t = dwell time in minutes.
40(mol) = moles corrected for blank and reactor-produced 40.
Ratios are corrected for blanks, decay and interference.
$\sum^{39}$Ar is cumulative, ^{40}Ar* = rad fraction.

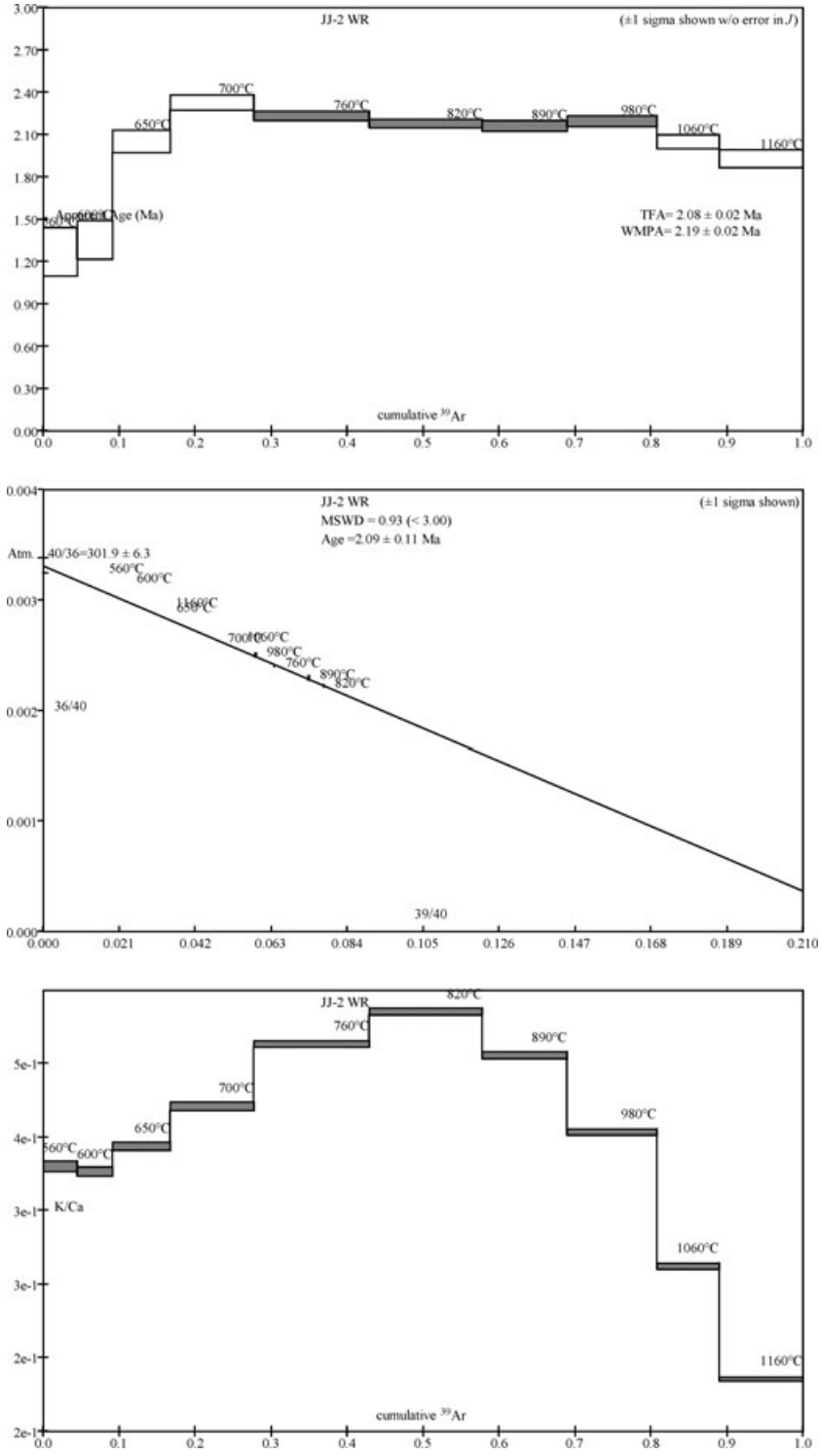

Sample:		SN53–11	JJ-3 WR		$J = 0.0002688$					
T	t	40(mol)	40/39	38/39	37/39	36/39	K/Ca	$\sum {}^{39}$Ar	^{40}Ar*	Age (Ma)
600	12	$5.0e^{-14}$	45.9659	$1.5e^{-3}$	1.2810	0.1424	0.38	0.05515	0.085	1.9 ± 0.1
720	12	$8.9e^{-14}$	24.2639	$0.0e^{+0}$	1.1090	0.0666	0.44	0.24139	0.189	2.2 ± 0.0
860	12	$5.5e^{-14}$	14.9583	$0.0e^{+0}$	0.9208	0.0350	0.53	0.42859	0.308	2.2 ± 0.0

940	12	$3.8e^{-14}$	18.4927	$0.0e^{+0}$	1.3173	0.0470	0.37	0.53270	0.248	2.2 ± 0.0
1020	12	$3.5e^{-14}$	21.7041	$0.0e^{+0}$	1.8628	0.0573	0.26	0.61478	0.220	2.3 ± 0.0
1100	12	$5.2e^{-14}$	32.0312	$0.0e^{+0}$	2.7160	0.0934	0.18	0.69715	0.139	2.2 ± 0.1
1160	12	$9.1e^{-14}$	54.5809	$9.9e^{-4}$	4.5764	0.1696	0.11	0.78214	0.082	2.2 ± 0.1
1210	12	$2.4e^{-13}$	57.0959	$4.8e^{-4}$	9.6545	0.1750	0.051	1.00000	0.094	2.6 ± 0.1

Total fusion age (TFA) $= 2.29 \pm 0.02$ Ma (including J)
Weighted mean plateau age (WMPA) $= 2.23 \pm 0.02$ Ma (including J)
Inverse isochron age $= 2.26 \pm 0.03$ Ma. (MSWD $= 1.37$; $^{40}Ar/^{36}Ar = 294.2 \pm 1.1$)
Steps used: 720, 860, 940, 1020, 1100, 1160 (2–7/8 or 73% $\sum {}^{39}Ar$
t = dwell time in minutes.
40(mol) = moles corrected for blank and reactor-produced 40.
Ratios are corrected for blanks, decay and interference.
$\sum^{39}Ar$ is cumulative, $^{40}Ar^*$ = rad fraction.

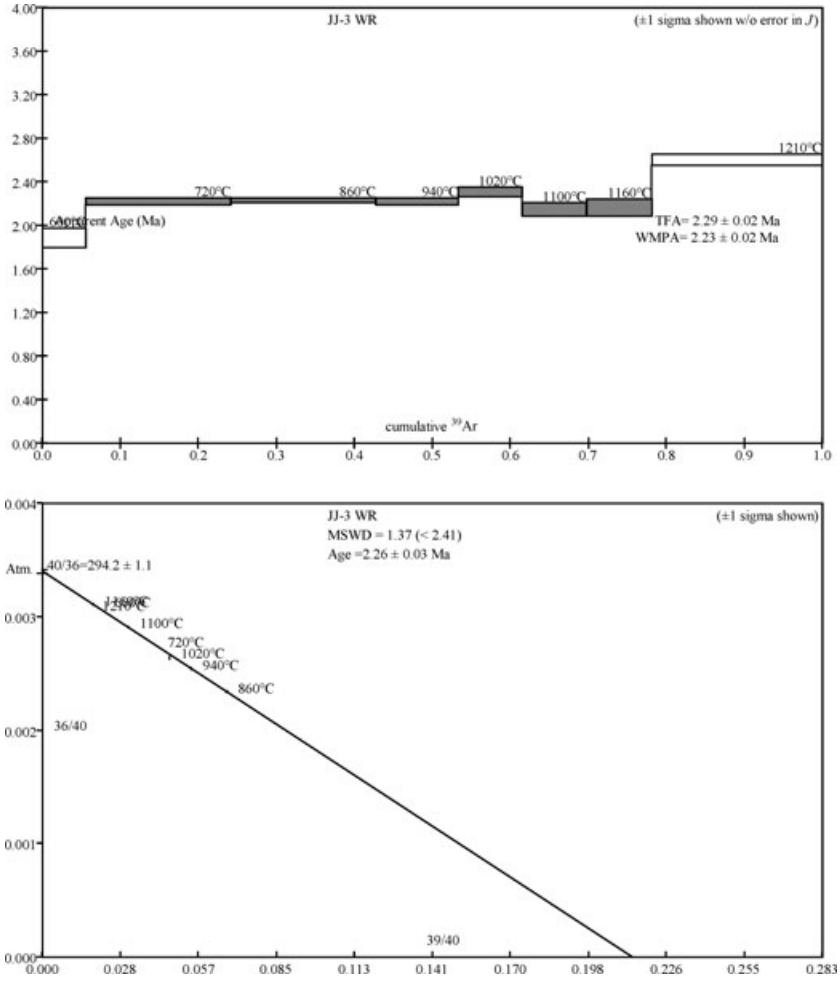

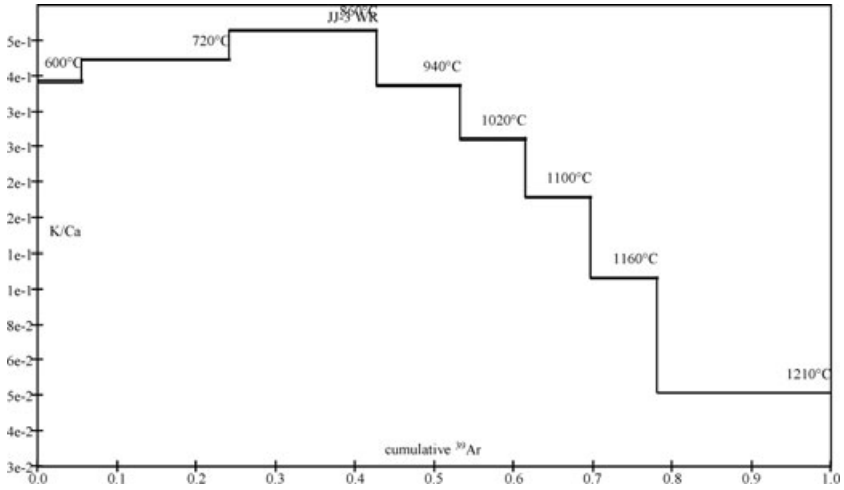

Sample:		SB53–12	AV-NEH WR		$J = 0.0002664$					
T	t	40(mol)	40/39	38/39	37/39	36/39	K/Ca	$\sum {}^{39}$Ar	^{40}Ar*	Age (Ma)
600	12	$6.9e^{-14}$	29.1998	$6.9e^{-4}$	1.0996	0.0870	0.45	0.12168	0.120	1.7 ± 0.0
700	12	$9.4e^{-14}$	17.6327	$0.0e^{+0}$	1.1457	0.0483	0.43	0.39632	0.191	1.6 ± 0.0
770	12	$5.2e^{-14}$	13.3851	$0.0e^{+0}$	0.8240	0.0341	0.59	0.59692	0.247	1.6 ± 0.0
920	12	$3.3e^{-14}$	20.3812	$0.0e^{+0}$	1.0700	0.0558	0.46	0.68051	0.190	1.9 ± 0.0
1000	12	$2.7e^{-14}$	19.8165	$0.0e^{+0}$	1.4459	0.0542	0.34	0.75042	0.192	1.8 ± 0.1
1070	12	$4.3e^{-14}$	22.4577	$0.0e^{+0}$	1.4279	0.0643	0.34	0.85051	0.154	1.7 ± 0.0
1150	12	$9.5e^{-14}$	32.9364	$0.0e^{+0}$	2.3797	0.0997	0.21	1.00000	0.106	1.7 ± 0.0

Total fusion age (TFA) = 1.67 ± 0.01 Ma (including J)
Weighted mean plateau age (WMPA) = 1.65 ± 0.01 Ma (including J)
Inverse isochron age = 1.56 ± 0.10 Ma. (MSWD = 9.13; ^{40}Ar/^{36}Ar = 299.2 ± 3.6)
Steps used: 600, 700, 770, 920, 1000, 1070, 1150 (1–7/7 or 100% $\sum {}^{39}$Ar
t = dwell time in minutes.
40(mol) = moles corrected for blank and reactor-produced 40.
Ratios are corrected for blanks, decay and interference.
$\sum^{39}$Ar is cumulative, ^{40}Ar* = rad fraction.

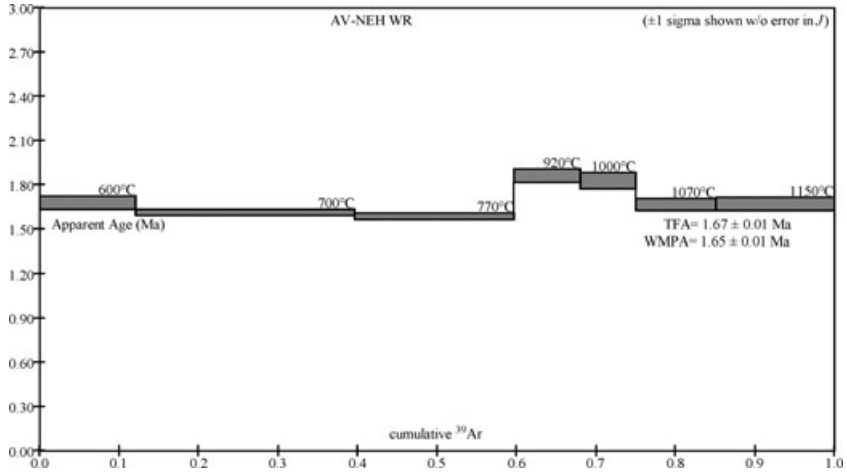

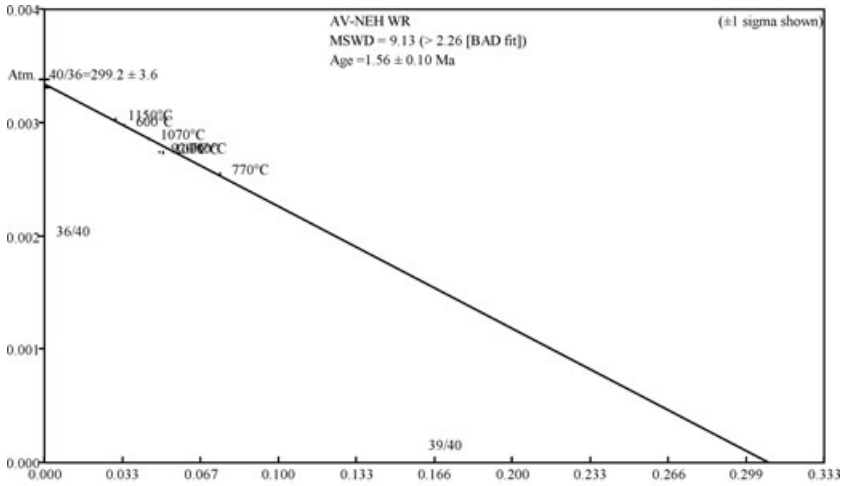

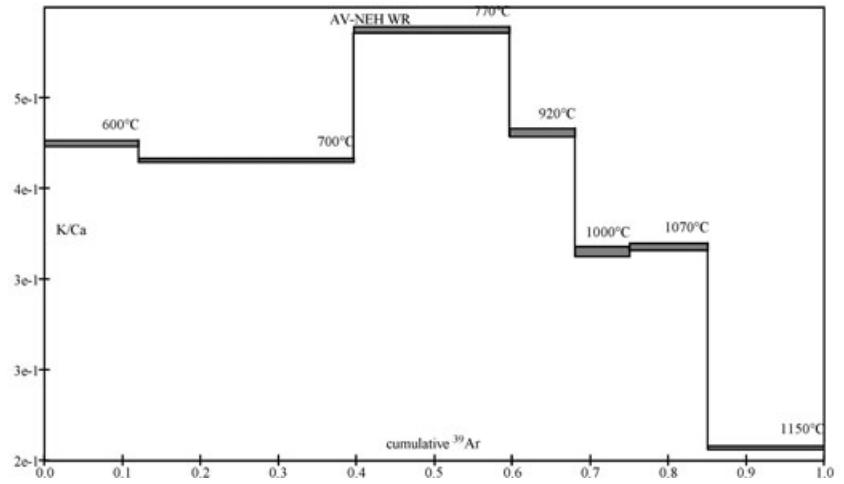

Sample:		SB53–16	Bv-NEH WR		$J = 0.0002585$					
T	t	40(mol)	40/39	38/39	37/39	36/39	K/Ca	$\sum {}^{39}$Ar	^{40}Ar*	Age (Ma)
650	12	$1.1e^{-15}$	13.5591	$0.0e^{+0}$	1.2428	0.0196	0.39	0.00741	0.572	3.6 ± 0.6
720	12	$6.5e^{-15}$	9.2624	$0.0e^{+0}$	0.8481	0.0130	0.58	0.06900	0.584	2.5 ± 0.1
790	12	$1.6e^{-14}$	7.3629	$0.0e^{+0}$	0.8575	0.0086	0.57	0.25477	0.654	2.2 ± 0.0
860	12	$2.0e^{-14}$	6.4155	$0.0e^{+0}$	1.2061	0.0090	0.41	0.53117	0.584	1.7 ± 0.0
930	12	$1.7e^{-14}$	7.1100	$0.0e^{+0}$	1.8261	0.0115	0.27	0.74707	0.520	1.7 ± 0.0
1000	12	$1.5e^{-14}$	10.4720	$1.9e^{-4}$	2.6316	0.0228	0.19	0.87276	0.357	1.7 ± 0.0
1070	12	$1.5e^{-14}$	20.2673	$2.0e^{-3}$	3.2081	0.0555	0.15	0.94021	0.191	1.8 ± 0.1
1140	12	$2.0e^{-14}$	29.1374	$0.0e^{+0}$	4.4716	0.0878	0.11	1.00000	0.110	1.5 ± 0.1

Total fusion age (TFA) = 1.88 ± 0.02 Ma (including J)
Weighted mean plateau age (WMPA) = 1.74 ± 0.02 Ma (including J)
Inverse isochron age = 1.73 ± 0.03 Ma. (MSWD = 0.33; ^{40}Ar/^{36}Ar = 297.7 ± 2.2)
Steps used: 860, 930, 1000, 1070 (4–7/8 or 69% $\sum {}^{39}$Ar
t = dwell time in minutes.
40(mol) = moles corrected for blank and reactor-produced 40.
Ratios are corrected for blanks, decay and interference.
$\sum^{39}$Ar is cumulative, ^{40}Ar* = rad fraction.

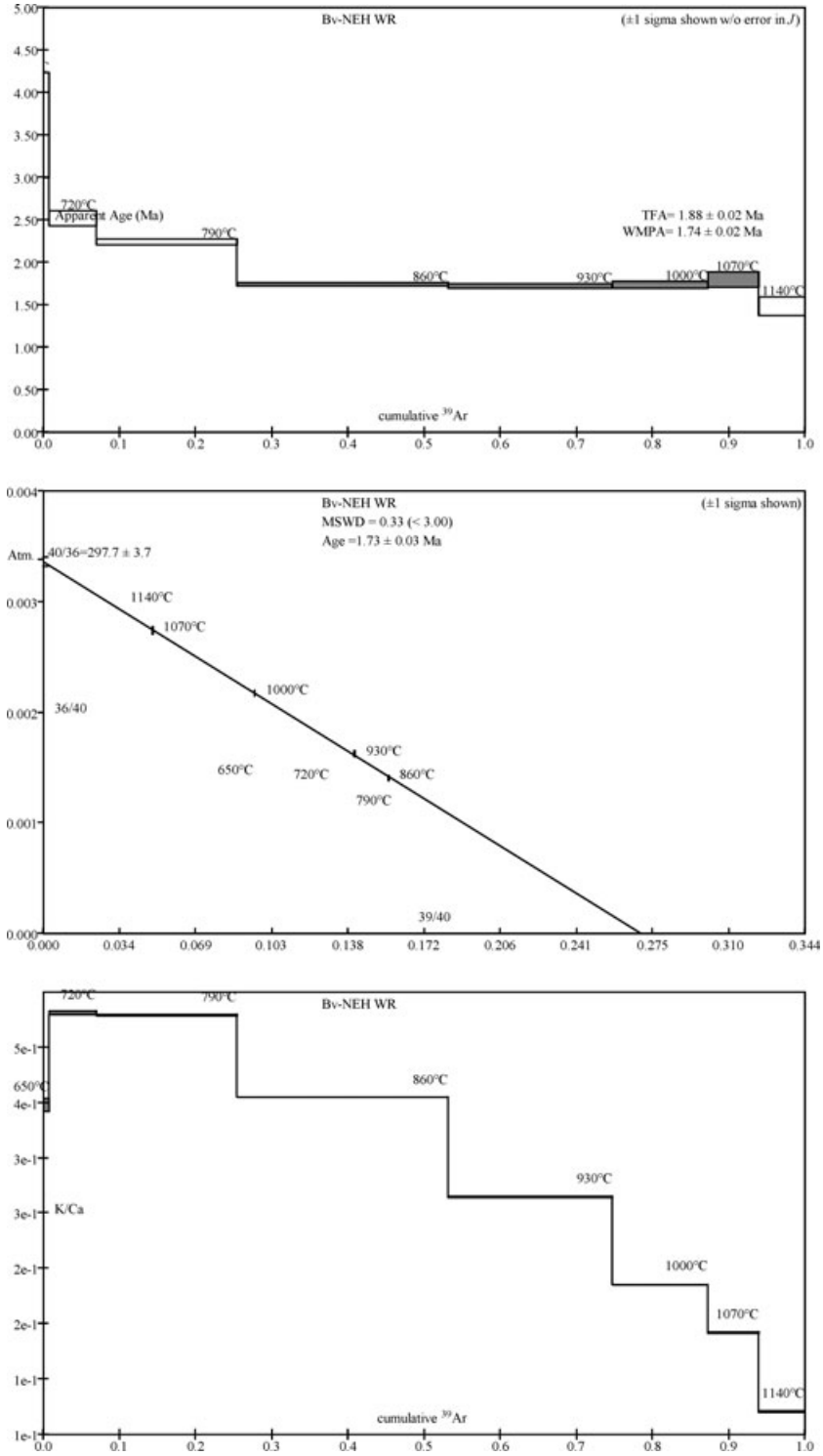

Sample:		SB53–6	CV-NEH WR		$J = 0.0002765$					
T	t	40(mol)	40/39	38/39	37/39	36/39	K/Ca	$\sum {}^{39}$Ar	^{40}Ar*	Age (Ma)
560	12	$6.0e^{-14}$	144.2041	$3.8e^{-3}$	1.6371	0.4588	0.30	0.03555	0.060	4.3 ± 0.4
600	12	$3.8e^{-14}$	81.5874	$2.8e^{-3}$	1.8110	0.2455	0.27	0.07556	0.111	4.5 ± 0.2
650	12	$4.3e^{-14}$	50.4608	$0.0e^{+0}$	1.8225	0.1382	0.27	0.14792	0.190	4.8 ± 0.1
700	12	$4.3e^{-14}$	34.7147	$6.9e^{-4}$	1.6695	0.0849	0.29	0.25485	0.277	4.8 ± 0.1
760	12	$4.8e^{-14}$	25.1186	$0.0e^{+0}$	1.3337	0.0521	0.37	0.41924	0.388	4.8 ± 0.0

820	12	$3.8e^{-14}$	20.7140	$0.0e^{+0}$	1.0084	0.0374	0.49	0.57768	0.467	4.8 ± 0.0
890	12	$3.3e^{-14}$	19.1277	$0.0e^{+0}$	1.0074	0.0320	0.49	0.72419	0.506	4.8 ± 0.0
980	12	$3.9e^{-14}$	27.3478	$3.4e^{-4}$	1.3509	0.0604	0.36	0.84458	0.348	4.7 ± 0.1
1060	12	$3.6e^{-14}$	37.5280	$8.2e^{-5}$	1.6574	0.0941	0.30	0.92581	0.259	4.8 ± 0.1
1160	12	$4.3e^{-14}$	49.6425	$0.0e^{+0}$	2.2346	0.1368	0.22	1.00000	0.186	4.6 ± 0.1

Total fusion age (TFA) = 4.76 ± 0.03 Ma (including *J*)
Weighted mean plateau age (WMPA) = 4.81 ± 0.03 Ma (including *J*)
Inverse isochron age = 4.83 ± 0.05 Ma. (MSWD = 0.73; $^{40}Ar/^{36}Ar = 294.9 \pm 1.2$)
Steps used: 650, 700, 760, 820, 890, 980, 1060 (3–9/10 or 85% $\sum {}^{39}Ar$
t = dwell time in minutes.
40(mol) = moles corrected for blank and reactor-produced 40.
Ratios are corrected for blanks, decay and interference.
$\sum^{39}Ar$ is cumulative, $^{40}Ar^*$ = rad fraction.

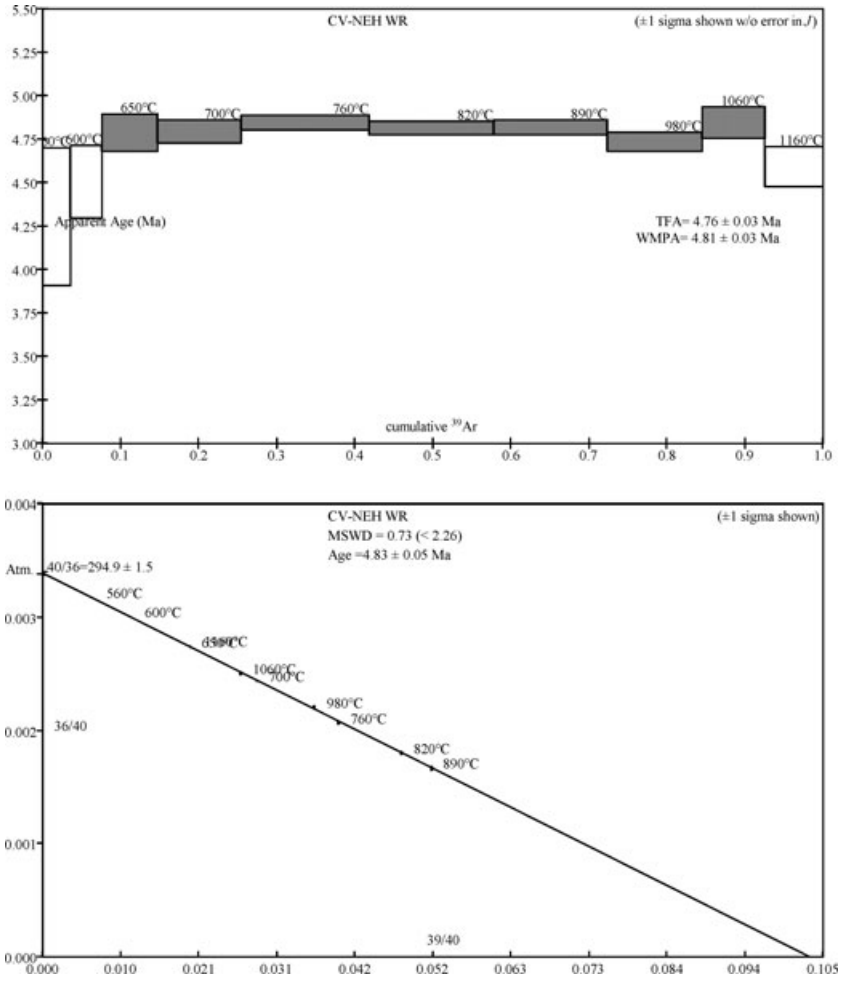

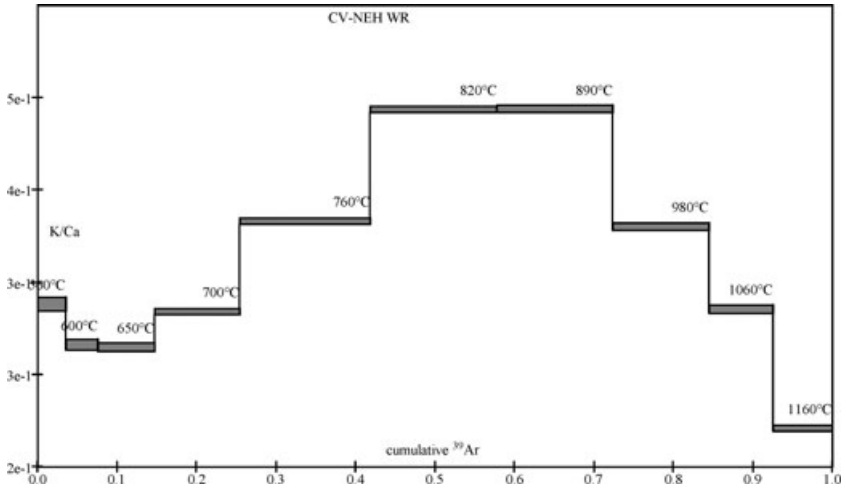

Sample:		SB53–3	NY-4 WR		$J = 0.0002793$					
T	t	40(mol)	40/39	38/39	37/39	36/39	K/Ca	$\sum{}^{39}$Ar	^{40}Ar*	Age (Ma)
560	12	$1.3e^{-13}$	184.1037	$1.3e^{-3}$	0.2307	0.4301	2.1	0.18946	0.310	28.5 ± 0.3
620	12	$1.0e^{-13}$	164.9799	$0.0e^{+0}$	0.4367	0.3605	1.1	0.34770	0.354	29.2 ± 0.3
700	12	$2.8e^{-14}$	116.3542	$2.0e^{-3}$	1.4357	0.2109	0.34	0.40927	0.464	27.0 ± 0.4
750	12	$4.2e^{-14}$	106.6948	$0.0e^{+0}$	1.0478	0.1734	0.47	0.51230	0.520	27.7 ± 0.2
890	12	$1.3e^{-13}$	105.2699	$0.0e^{+0}$	0.5335	0.1712	0.92	0.83692	0.519	27.3 ± 0.2
1050	12	$6.1e^{-14}$	257.8424	$0.0e^{+0}$	1.0089	0.7005	0.49	0.89839	0.197	25.4 ± 0.7
1150	12	$1.1e^{-13}$	275.0813	$2.7e^{-3}$	1.1283	0.7641	0.43	1.00000	0.179	24.7 ± 0.6

Total fusion age (TFA) $= 27.48 \pm 0.16$ Ma (including J)
Weighted mean plateau age (WMPA) $= 27.40 \pm 0.15$ Ma (including J)
Inverse isochron age $= 28.81 \pm 2.67$ Ma. (MSWD $= 4.49$; ^{40}Ar/^{36}Ar $= 279.2 \pm 31.0$)
Steps used: 700, 750, 890 (3–5/7 or 49% $\sum{}^{39}$Ar
t = dwell time in minutes.
40(mol) = moles corrected for blank and reactor-produced 40.
Ratios are corrected for blanks, decay and interference.
$\sum^{39}$Ar is cumulative, ^{40}Ar* = rad fraction.